AIAA JOURNAL
Vol. 49, No. 2, February 2011

Numerical Simulation of Two-Dimensional Acoustic Liners with High-Speed Grazing Flow

Qi Zhang* and Daniel J. Bodony†
University of Illinois at Urbana-Champaign, Urbana, Illinois 61801

DOI: 10.2514/1.J050597

Resonant acoustic liners are used to dissipate acoustic energy in engine ducts in the presence of grazing flow. Future applications have been proposed that will expose liners to much higher grazing flow velocities than are typically encountered. To study their characteristics at these conditions, a fully predictive liner eduction technique is developed by solving the compressible Navier–Stokes equations with accurate boundary conditions. Validation of the numerical approach is demonstrated by comparing the predicted absorption characteristics of a 3 kHz resonant liner geometry without any background flow against existing computational and experimental data. Using the validated approach, simulations at more realistic liner operating conditions are performed. Incident grazing acoustic waves of different intensity and frequency are performed at grazing flow Mach numbers up to 0.85. The liner impedance is evaluated and compared with existing semiempirical models; reasonable agreement is found in most cases. The simulation databases are then used to examine candidate quantities for recently suggested time-domain liner models. It is found that, at high grazing Mach numbers, the vortex shedding characteristics continue to be a strong function of frequency, with incident waves of lower frequency leading to stronger vortex shedding. It is also found that the aperture wall shear stress and displacement thickness are strongly coupled to the in-aperture flow details, while the mass flux through the aperture is more closely linked to the incident sound frequency.

Nomenclature

a	=	speed of sound
D	=	diameter of liner aperture
d	=	thickness of facesheet plate
k	=	acoustic wave number, $2\pi/\lambda$
H	=	depth of cavity
p	=	thermodynamic pressure
R	=	acoustic resistance
T	=	period of oscillation
X	=	acoustic reactance
Z	=	acoustic impedance, $R + iX$
z	=	normalized acoustic impedance, $Z/(\rho_\infty a_\infty)$
γ	=	ratio of specific heats
$\Delta\phi_i$	=	phase correction for pressure signal measured at position A_i
δ_1	=	displacement thickness, $\int_0^\infty [1 - (\rho u)/(\rho_{\text{ref}} u_{\text{ref}})]\,\mathrm{d}y$
δ_{99}	=	boundary-layer thickness, where $U(\delta_{99})/u_{\text{ref}}$ is 0.99
ζ	=	planar vorticity, $\partial v/\partial x - \partial u/\partial y$
Θ	=	temperature
θ	=	normalized acoustic resistance, $R/(\rho_\infty a_\infty)$
κ	=	thermal conductivity
λ	=	wavelength
μ	=	first coefficient of fluid viscosity
μ_B	=	bulk viscosity
ρ	=	density
σ	=	porosity of perforated facesheet
τ_{ij}	=	viscous stress tensor
τ_w	=	wall shear stress
ϕ_{AB}	=	phase difference between pressure signal measured at points A and B
χ	=	normalized acoustic reactance, $X/(\rho_\infty a_\infty)$
ψ	=	planar incident wave angle (made with vertical $+y$ axis)
ω	=	circular frequency, $2\pi f$
$(\cdot)_{\text{ref}}$	=	reference quantity
$(\cdot)_\infty$	=	ambient variable
$(\cdot)^*$	=	dimensional variable
$\overline{(\cdot)}$	=	phase-averaged quantity

Received 7 April 2010; revision received 28 October 2010; accepted for publication 1 November 2010.

*Research Assistant, Department of Aerospace Engineering, 104 South Wright Street, 326 Talbot Laboratory.

†Assistant Professor, Department of Aerospace Engineering, 104 South Wright Street, 313 Talbot Laboratory. Senior Member AIAA.

I. Introduction

ACOUSTIC liners play an important role in aircraft gas turbine engine noise reduction by converting acoustic fluctuations into nonradiating vortical disturbances through small openings, or apertures, in a perforated facesheet backed by a cavity for which the depth is tuned to provide attenuation over a range of frequencies. Their performance is typically characterized by a frequency-dependent acoustic impedance Z for which the complex value relates the damping and phase change an acoustic wave undergoes after interaction with the liner. Determining Z for a given liner design is a critical step toward its on-vehicle application, and several methods exist to do so, mostly based on empirical measurement coupled with inverse techniques. It has been proposed that liners be used on exterior vehicle surfaces, typically near buried or podded engine exits, as a means of further reducing the acoustic impact of next generation vehicles. The proposed usage occurs at conditions not typically seen by liners and represents an experimental and modeling challenge to educe a liner's impedance at these conditions. The present work builds upon existing liner eduction methodologies by considering their application in high-speed grazing flows, up to Mach 0.85, through a fully predictive approach and assessing necessary modeling changes, using both frequency and time-domain concepts.

Conventional aircraft engine duct acoustic liners can be classified into three types: 1) single-degree-of-freedom (SDOF) liners, 2) two-degree-of-freedom liners (2DOF), and 3) bulk absorbers. SDOF liners are most effective for narrow frequency ranges, while bulk absorbers are more effective for broadband sound [1]. However, due to construction difficulties, bulk absorber liners are seldom applied in commercial aircraft. 2DOF liners have also seen limited use, and most installed liners are of the SDOF type. As there exists a wide range of possible factors that may affect the performance of acoustic liners, most studies have been restricted to the SDOF liners.

Relatively simple SDOF liners exhibit complicated fluid mechanical behavior that is not completely understood. Early experiments, which focused on the fluid mechanical aspects of small apertures, found that the aperture size significantly influenced the role of viscosity on the in-aperture flow and may, if small enough, inhibit the oscillatory jet's transition to a turbulent state [2], an idea also linked to the incident sound amplitude by Melling [3]. Melling also suggested a semiempirical method for evaluating a liner's impedance and its (possibly) nonlinear dependence on the sound amplitude. In doing so, he proposed that for low intensity sound waves, wall friction around the resonator opening is the principle dissipation mechanism, while for high intensity sound waves, an oscillatory turbulent jet was found right at the entrance of the resonator. These observations were built into an impedance model by Hersh and Rogers [4]. An impedance measurement technique for when a grazing flow was present was proposed by Dean [5], which has found wide application because of its simplicity and reliability. This technique has been shown to be capable of impedance evaluations over a range of flow conditions to an accuracy of 10% or better and can be applied when a grazing flow exists. Rice [6] included the effects of a steady grazing flow, argued that the grazing flow dominated the near-aperture dynamics, and developed an impedance model based on this assumption. A quasi-steady model developed by Howe [7] used a steady vortex sheet model to account for the flow separation off the aperture walls to provide the acoustic-to-vortical scattering such that the acoustic dissipation was linearly proportional to its amplitude. Zorumski and Tester [8] reviewed the prediction of the acoustic impedance of duct liners at the time, including both linear and nonlinear effects, the presence of grazing flow, and the properties of the facesheet or bulk-type materials. Several methods for predicting the properties of single or multilayered, point reacting or extended reaction, and flat or curved liners were also discussed.

Jing and Sun [9] and Jing et al. [10] investigated experimentally perforated liners with grazing flow and found that the presence of the grazing flow can markedly increase both the absorption coefficient and effective bandwidth of a perforated liner. They also showed that the plate thickness has a major influence on the acoustic properties of a liner with bias flow. A simple empirical model was proposed with good agreement of the experimental data; however, their investigations are mostly at low sound pressure levels (SPLs) to avoid nonlinear effects.

Liners with a net bias flow through the aperture are also useful. Hughes and Dowling [11] and Dowling and Hughes [12] studied vortex shedding from screens of regular arrays of slits and circular perforations and showed that it is theoretically possible to absorb all impinging sound at a particular frequency if a rigid backing wall was included such that reflection from the wall allowed for substantially more interaction between the sound and screen. Later, Eldredge and Dowling [13] conducted an experiment concerning the effectiveness of such a liner in a circular duct to absorb planar acoustic waves. A one-dimensional model of the absorption mechanism was developed using a homogeneous liner compliance. The model was evaluated by comparing with experimental results, and excellent agreement was found. It is noted that their system can absorb a large fraction of incoming energy, and it can prevent all of the energy produced by an upstream source in certain frequency ranges from reflecting back of planar acoustic waves. Moreover, the increase of the bandwidth of this strong absorption can be achieved by appropriate placement of the liner system in the duct.

Aside from the modeling of liner impedance, determining its value in a complex flow has resulted in a number of semiempirical approaches to liner eduction. In simple no-flow cases where normally incident plane waves interact with a liner, reflected and transmitted wave amplitudes can be used to determine the impedance. For more complicated flows, Dean [5] proposed a two-microphone method, which has found wide application because of its simplicity and reliability, even in the presence of grazing flows. Inverse methods have been developed that combine pressure measurements in the vicinity of the liner (usually upstream, downstream, and above with a description of the propagation, such as the convected Helmholtz equation) try to find the wall impedance values that most closely match the measured data [14]. More recent inverse techniques have focused on increasing the fidelity of the physical model by moving toward the linearized Euler equations from the convected wave equation [15–19].

The insight gained from theoretical and/or experimental studies has recently been complemented with numerical studies of liner behavior, most of which have focused on the near-aperture fluid mechanics. Tam and Kurbatskii [20], for example, performed a series of numerical simulations of 2-D resonant liners without flow, where they observed two different acoustic energy conversion mechanisms, depending on the sound amplitude, as suggested earlier [3]. The simulation predictions were later compared with experimental data [21] using the absorption coefficient as a metric instead of the impedance. Further 2-D simulations by Tam et al. [22] were performed in a joint numerical–experimental study of slit liners of different geometries at various incident sound frequencies. They observed that significant vorticity is shed from 45° beveled slits, regardless of whether the fluid is entering or exiting the cavity, and always followed by inviscidly unstable thin shear layers. For 90° corners, the vortex shedding ceases when SPL is reduced below a threshold, but for 45° corners, vortex shedding continues to a lower SPL threshold. Thus, they argue, resonators with 45° corners are more efficient in acoustic energy dissipation than 90° corners. The introduction of a low-speed laminar boundary layer as a base flow in two-dimensional (2-D) slit resonator numerical simulation was performed by Tam et al. [23], with more recent simulations focusing on three-dimensional (3-D) rectangular orifice liners without grazing flow [24]. The only simulations to include a turbulent boundary were performed by Eldredge et al. [25], who examined a multiperforated liner with bias flow using an incompressible large-eddy simulation methodology. By comparing with the theoretical model of Howe [26], their simulation results demonstrated that Howe's model for the Rayleigh conductivity of the aperture provides a reasonable estimate of the impedance at small frequencies but loses accuracy at higher frequencies.

The present work examines the behavior of 2-D resonator liners but extends the analysis to a high-speed grazing flow, up to Mach 0.85, and directly computes the liner impedance using Dean's method [5]. The location of the microphones is found to be increasingly important as the grazing flow velocity increases, as does the asymmetry in the aperture response. A discussion of the time-domain dependence of liner model quantities proposed by Hersh et al. [27] is also provided, where a single frequency response is not found in all measured quantities. Finally, the Mach number dependence of the liner impedance is examined using existing semiempirical models [6,28] as a guide, where their functional form is found to yield reasonable predictions at high Mach numbers.

Our discussion begins with a description of the numerical method used, followed by its validation in a case without grazing flow, considered previously [21]. The validation is then extended to low-speed grazing flow using impedance data for a rectangular slit liner, taken by Jing et al. [10]. Predictions at higher grazing flow Mach numbers are then presented, and their data are analyzed with respect to changes in incident wave frequency and amplitude and the grazing flow velocity. The results conclude by presenting curve fits for phase-averaged time-domain quantities. A summary of the work is then given.

II. Numerical Method

The simulations used an in-house code to solve the nondimensional equations of a compressible viscous fluid:

$$\frac{\partial \rho}{\partial t} + \frac{\partial}{\partial x_j}\rho u_j = 0 \tag{1}$$

$$\frac{\partial \rho u_i}{\partial t} + \frac{\partial}{\partial x_j}(\rho u_i u_j + p\delta_{ij} - \tau_{ij}) = 0 \tag{2}$$

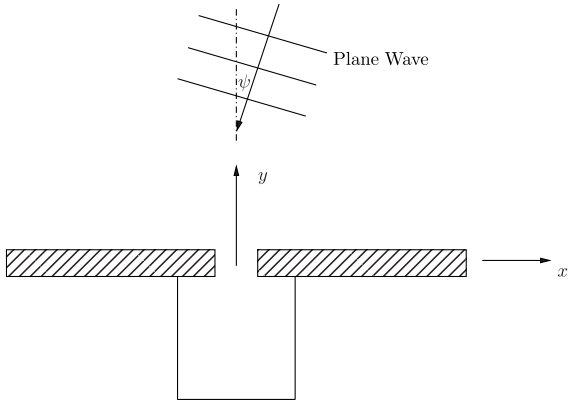

Fig. 1 Schematic of the no-flow validation study of normally incident waves propagating in a quiescent medium.

$$\frac{\partial \rho E}{\partial t} + \frac{\partial}{\partial x_j}(\{\rho E + p\}u_j + q_j - u_i \tau_{ij}) = 0 \tag{3}$$

A Newtonian fluid and a Fourier heat conduction model are assumed, such that the viscous stress tensor and heat flux, respectively, are

$$\tau_{ij} = \frac{\mu}{Re}\left(\frac{\partial u_i}{\partial x_j} + \frac{\partial u_j}{\partial x_i}\right) + \frac{1}{Re}\left(\mu_B - \frac{2}{3}\mu\right)\frac{\partial u_k}{\partial x_k}\delta_{ij}$$

$$q_i = -\frac{\mu}{PrRe}\frac{\partial \Theta}{\partial x_i}$$

where the nondimensional variables are given by

$$t = \frac{t^*_\infty}{d^*/a^*_\infty}, \qquad x_i = \frac{x^*_i}{d^*}, \qquad \rho = \frac{\rho^*}{\rho^*_\infty}, \qquad u_i = \frac{u^*_i}{a^*_\infty}$$

$$p = \frac{p^*_\infty}{\rho^*_\infty a^{*2}_\infty}, \qquad \mu = \frac{\mu^*}{\mu^*_\infty}, \qquad \mu_B = \frac{\mu^*_B}{\mu^*_\infty}, \qquad \Theta = \frac{\Theta^*}{(\gamma-1)\Theta^*_\infty}$$

The bulk viscosity for air is used, $\mu_B = 0.6\mu$. The Reynolds number and Prandtl number are defined as

$$Re = \frac{\rho^*_\infty a^*_\infty d^*}{\mu^*_\infty}, \qquad Pr = \frac{C^*_p \mu^*_\infty}{\kappa^*_\infty}$$

with $Pr = 0.72$ for all of the simulations. A power-law model was assumed for the transport coefficients; namely,

$$\mu = [(\gamma - 1)\Theta]^n$$

where $n = 0.666$.

The incident acoustic waves have amplitude A and propagate at an angle ψ (see Fig. 1) to the vertical $+y$ axis. It is assumed that the incident sound is of the form of linear, monochromatic plane waves given by

$$\begin{bmatrix} \rho^i \\ u^i \\ v^i \\ p^i \end{bmatrix} = \begin{bmatrix} 1 \\ -\sin\psi \\ -\cos\psi \\ 1 \end{bmatrix} A\cos[-\omega(x\sin\psi + y\cos\psi + t)] \tag{4}$$

where A is related the decibel level by $A = 10^{\mathrm{SPL}/20 - 9.701}$. This formulation is identical to that used by Tam and Kurbatskii [20].

The spatial derivatives for $\partial/\partial x_i$ and $\partial^2/\partial x_i \partial x_i$ were discretized using a 3-4-6 Padé scheme [29]. Cross derivatives $\partial^2/\partial x_i \partial x_j$, with $i \neq j$, were computed using repeated first derivatives. The temporal integration used the standard fourth-order Runge–Kutta method. The boundary conditions used an extended version of the Poinsot and Lele [30] treatment found in Bodony [31]. Additional sponge zones [32,33] were used to minimize acoustic reflections and to help impose the acoustic forcing by adding a term $-\sigma(q - q_{\mathrm{ref}})$ to Eqs. (1–3), where $q = \{\rho, \rho u_i, \rho E\}$ and q_{ref} is the target, or reference state, far away from the liner, including the acoustic field in Eq. (4).

III. Validation for Liner Without Grazing Flow

Before investigating the resonant liners in a high-speed flow, the numerical methodology was validated on a no-flow case. The validation model chosen was that of [21], as shown in Fig. 2, which

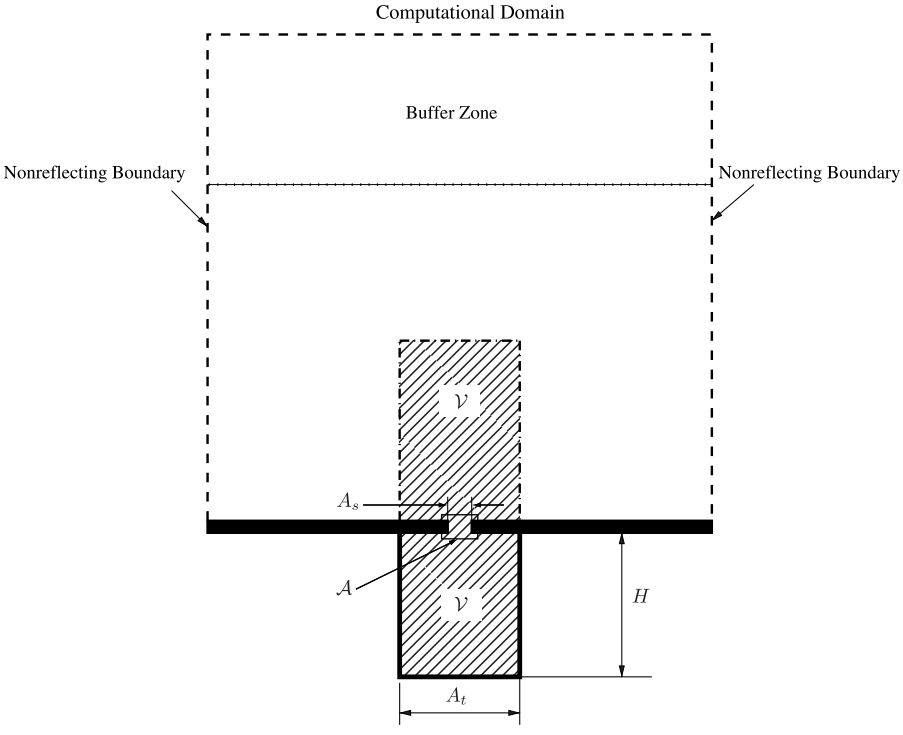

Fig. 2 Computational domain for first validation study showing boundary conditions and integration volumes.

included numerical and experimental data. We only consider the case of locally reacting acoustic liners where no communication between liners is possible. Because only absorption coefficients were available in [21] we focus on how they were calculated in the present case, which differs from that used in the reference work. Direct prediction of liner impedance will be given in Sec. IV.

The geometry of the liner is as follows and shown in Fig. 2. The aperture diameter A_s and facesheet thickness are 1 mm and are backed by a rectangular cavity of width $A_t = 14$ mm and depth $H = 35$ mm. Based on the ambient density, speed of sound, and aperture diameter, the Reynolds numbers is roughly 19,000. The domain height above the facesheet was of height $150A_s$, while the width was $75A_s$. The left and right boundaries used nonreflecting boundary conditions, while the upper boundary was used to send acoustic waves into the domain via a characteristic boundary condition and the sponge layer. All solid walls were no-slip and isothermal and kept at a temperature of 15°C.

Once the response of the fluid near the aperture reached a statistically steady state, which took roughly 20 forcing periods, the flowfield was saved as a time-resolved database for later processing. Using the database and the same numerical schemes given in Sec. II, it is straightforward to calculate the viscous dissipation. The time-averaged dissipation at position (x, y) is given by

$$\bar{D}(x,y) = \frac{1}{T}\int_0^T \tau_{ij}\frac{\partial u_i}{\partial x_j}\,\mathrm{d}t \tag{5}$$

where T is the period of oscillation, and the integrand is the instantaneous viscous dissipation. Tam and Kurbatskii [20], to whose work we compare, argue that the total acoustic energy dissipation rate, denoted by $E_{\text{dissipation}}$, is closely related to the mechanisms of the flowfield such that the dissipation mechanisms were either due to wall losses or the scattering of sound into vorticity. In this spirit, the acoustic dissipation rate is defined as

without vortex shedding:

$$E_{\text{dissipation}} \approx E^{\mathcal{A}}_{\text{viscous}} \tag{6}$$

with vortex shedding:

$$E_{\text{dissipation}} \approx E^{\mathcal{A}}_{\text{viscous}} + E_{\text{shedding}} \tag{7}$$

where superscript $\mathcal{A}$ denotes the area region in the immediate vicinity of the liner aperture, and $E^{\mathcal{A}}_{\text{viscous}}$ is the viscous dissipation in this region (see Fig. 2). By integrating Eq. (5) in region $\mathcal{A}$, the viscous dissipation rate in the aperture region of the liner is found to be

$$E^{\mathcal{A}}_{\text{viscous}} = \iint_{\mathcal{A}} \bar{D}(x,y)\,\mathrm{d}x\,\mathrm{d}y \tag{8}$$

To evaluate E_{shedding}, representing the conversion of acoustic energy by scattering, Tam and Kurbatskii [20] counted the number of vortices N created in time T and assumed each vortex carried the same amount of kinetic energy K, such that the total kinetic energy bound vortices, per unit time, are KN/T. Under the assumption that the bound kinetic energy comes solely from the sound field, Tam and Kurbatskii suggest that

$$E_{\text{shedding}} = \frac{KN}{T} \tag{9}$$

Such a definition requires the counting and tracking of individual vortices throughout the simulation, estimating their size, rotation, and kinetic energy and does not generalize to flows with turbulence or other forms of bound energy.

In contrast, we evaluate the dissipation rate by its definition over a large enough integral domain (see Fig. 2, denoted by $\mathcal{V}$). The assumption here is that the sole power input into the system arises from the incident sound, and that losses through the isothermal walls are negligible. In this case, the difference at steady state between the input and output powers is caused by dissipation, where the total viscous dissipation rate $E^{\mathcal{V}}_{\text{viscous}}$ can be directly calculated by integrating Eq. (5) over the region $\mathcal{V}$

$$E^{\mathcal{V}}_{\text{viscous}} = \iint_{\mathcal{V}} \bar{D}(x,y)\,\mathrm{d}x\,\mathrm{d}y \tag{10}$$

Because the acoustic field is the sole power input, we then equate its rate of decrease with the viscous dissipation $E_{\text{dissipation}} = E^{\mathcal{V}}_{\text{viscous}}$. It was verified in Zhang [34] that the dissipation calculated using Eq. (10) was equal to the net difference between the incident and reflected sound power for the current data.

It is straightforward to evaluate the energy flux of the incident acoustic waves through an area A_s to the aperture of the resonator as

$$E_{\text{incident}} = \frac{\overline{(p_i')^2}A_s}{\rho_\infty a_\infty} \tag{11}$$

Based on Eq. (11), the area-weighted absorption coefficient, which measures the fraction of total sound power absorbed per unit depth, is given by

$$C_{\text{abs}} = \frac{E_{\text{dissipation}}}{E_{\text{incident}}}\frac{A_s}{A_t} \tag{12}$$

where A_s and A_t are the area of the liner aperture and area of the resonator, respectively, and shown in Fig. 2. The area weighting is required for valid comparison with the experimental data taken in Tam et al. [21], which have different porosities than do the simulations and is the same definition used in the computational portion in [21].

Figure 3 shows a comparison of the absorption coefficients measured experimentally and the numerical results calculated by Tam et al. [21]. As is evident, except for the 6 kHz case, the agreement with the experimental data is reasonable. It also shows a continuous decrease in the absorption coefficient, with increasing frequency until 5 kHz, after which there appears to be an increase. For $f \leq 5$ kHz, the continual decrease is tied to the decreased amount of vorticity production with increasing frequency and illustrates the utility of vortex shedding as an acoustic energy reduction mechanism.

Note that, also in Fig. 3, uncertainty bars are associated with each value of C_{abs}. These bars indicate the range of C_{abs} values obtained when different cycles were considered. In general, the uncertainty decreases with increasing frequency. (No bar is shown for the 1 kHz result.) It is interesting to point out that the discrepancy between the experimental and numerical data for the 6 kHz case is found in both Tam et al. [21] and in the present numerical investigations.

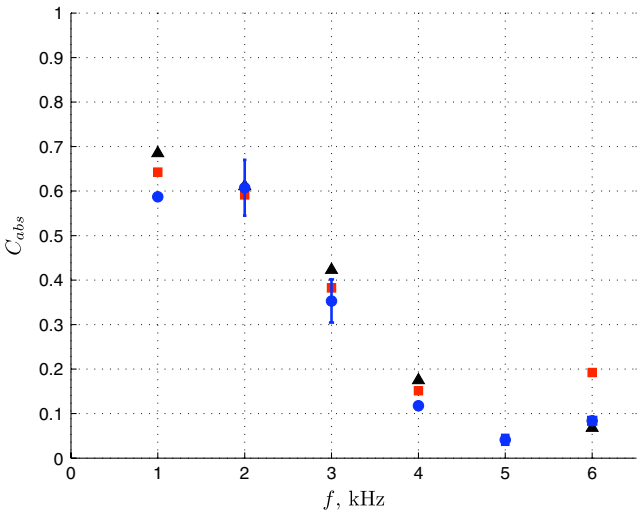

Fig. 3 Absorption coefficient as a function of frequency for a 150 dB incident sound wave (▲: Tam and Kurbatskii [20] numerical results; ■: experimental data in Tam et al. [21]; ●: present numerical results, with uncertainty bars).

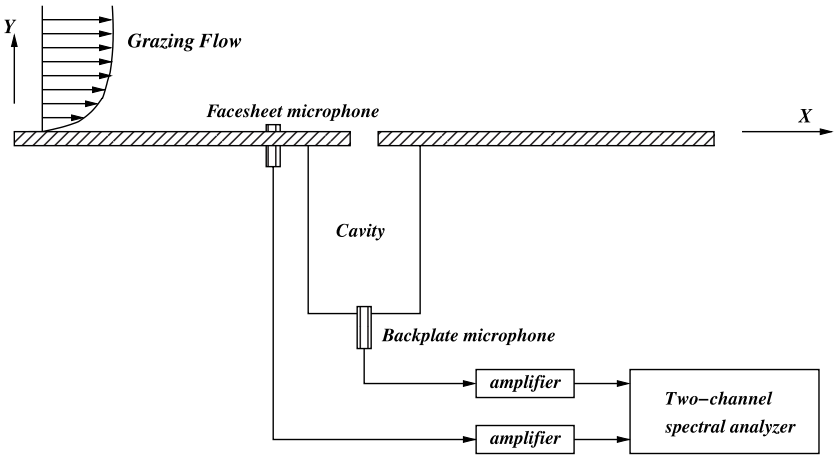

Fig. 4 Schematic of measurement of grazing flow impedance by the two-microphone method.

IV. Liner with Grazing Incidence and Grazing Flow

With the approach validated without a grazing flow, liners in grazing flow conditions are considered next. There are limited slit liner experimental data available that can be used to validate a 2-D simulation, but one relevant case was investigated by Jing et al. [10] for low grazing flow Mach numbers up to 0.15. There are three key differences between the Jing et al. experiment and the current simulation. First, the simulations are 2-D, whereas the experiment was obviously 3-D. The experimental case to which we compare is a rectangular, slit liner (case 5 of [10]) of modest aspect ratio. It is reasonable to suppose that a rectangular aperture behaves approximately 2-D when the grazing flow approaches the aperture normal to the long dimension or in the absence of flow, similar to the validation in Sec. III. The second distinction is that the boundary layers, when a grazing flow is present, are turbulent in the experiment, whereas ours are confined to be laminar. An impact of a turbulent boundary layer is to superimpose a hydrodynamic pressure fluctuation onto those associated with the acoustic field. At low Mach numbers, the hydrodynamic fluctuations scale like M_∞^2 and are much smaller in amplitude than in the applied acoustic field, a fact exploited by the liner model developed by Jing et al., such that the main impact of the turbulent boundary layer is its altered mean velocity profile. The third and final difference has to do with the incident sound waves. In the experiment, a speaker was placed above the aperture, whereas the simulation used grazing incidence. For the low frequencies and low Mach numbers considered here, the spatial wavelength of the sound was at least 150 times the aperture diameter, such that the phase of the incident pressure was constant over the aperture. In such a situation, the aperture cannot distinguish between grazing and normal incidence.

We proceed by predicting the impedance for zero and low-speed grazing flow to provide additional validation, then we examine the liner response as the grazing Mach number is increased to 0.85.

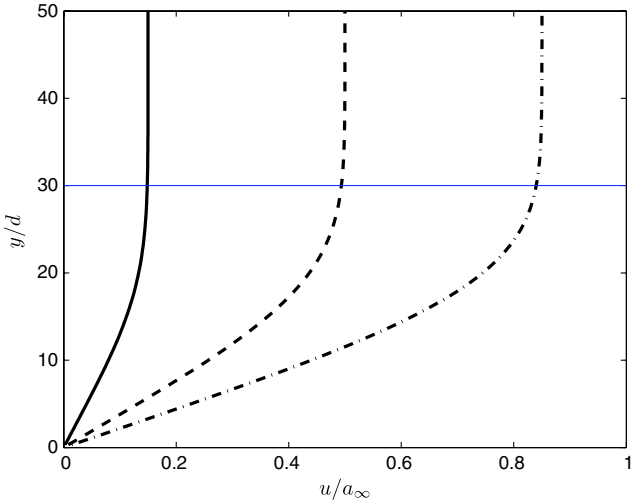

Fig. 5 Streamwise velocity profile within the compressible boundary layer (solid line: $M_\infty = 0.15$; dashed line: $M_\infty = 0.50$; dashed–dotted line: $M_\infty = 0.85$).

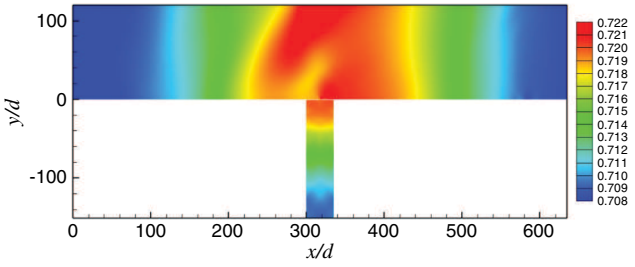

Fig. 6 Nondimensional pressure contours $p/(\rho_\infty a_\infty^2)$ of 1 kHz, 150 dB incident plane wave imposed on a $M_\infty = 0.85$ grazing flow.

A. Physical Model

Figure 4 provides a schematic figure of the physical setup. A self-similar zero pressure gradient compressible laminar boundary layer is introduced from the left. The freestream and wall temperatures are

Table 1 Numerical simulation cases performed

No.	SPL, dB	Incident frequency, Hz	Grazing Mach number, M_∞
1	130	500	0.00
2	130	500	0.15
3	150	500	0.15
4	150	500	0.50
5	150	500	0.85
6	150	1000	0.15
7	150	1000	0.50
8	150	1000	0.85

Table 2 Measurement points at different locations upstream of the aperture

No.	Label	d_i
0	A	0.0
1	A_1	15.9
2	A_2	21.3
3	A_3	30.0
4	A_4	42.5

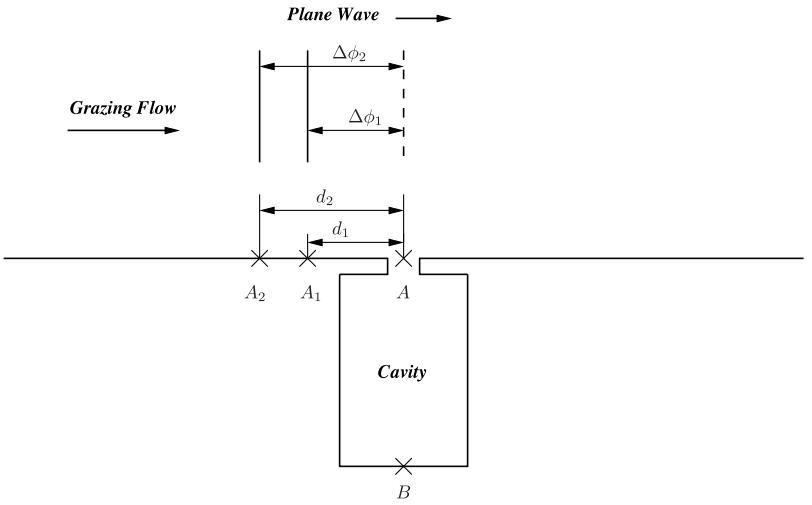

Fig. 7 Schematic of phase correction method.

held fixed at 300 K; the working gas was air at atmospheric pressure. The depth and width of the cavity are 150 and 35 mm, respectively. The facesheet thickness, also the reference length scale, are 1 mm and yield a Reynolds number of approximately 23,000 based on ambient quantities. The streamwise dimension of the aperture is 2 mm. The incident sound is imposed at the inlet of the duct, in the direction of the grazing flow; that is, we take $\psi = -\pi/2$ in Eq. (4). The visual boundary-layer thickness, δ_{99}, is 30 mm. Figure 5 shows the streamwise velocity profile of the compressible boundary layer for the three Mach numbers considered. The same visual boundary-layer thickness was used in all cases and is 15 times the aperture diameter. Figure 6 shows an example instantaneous pressure field inside the cavity and in the duct when the 1 kHz, 150 dB plane wave is imposed onto a grazing flow with $M_\infty = 0.85$. The set of simulation cases run is listed in Table 1.

The computational setup for the grazing flow simulations was very similar to that for the no-flow validation simulation of the previous section. The entire computational domain is shown in Fig. 6. At the

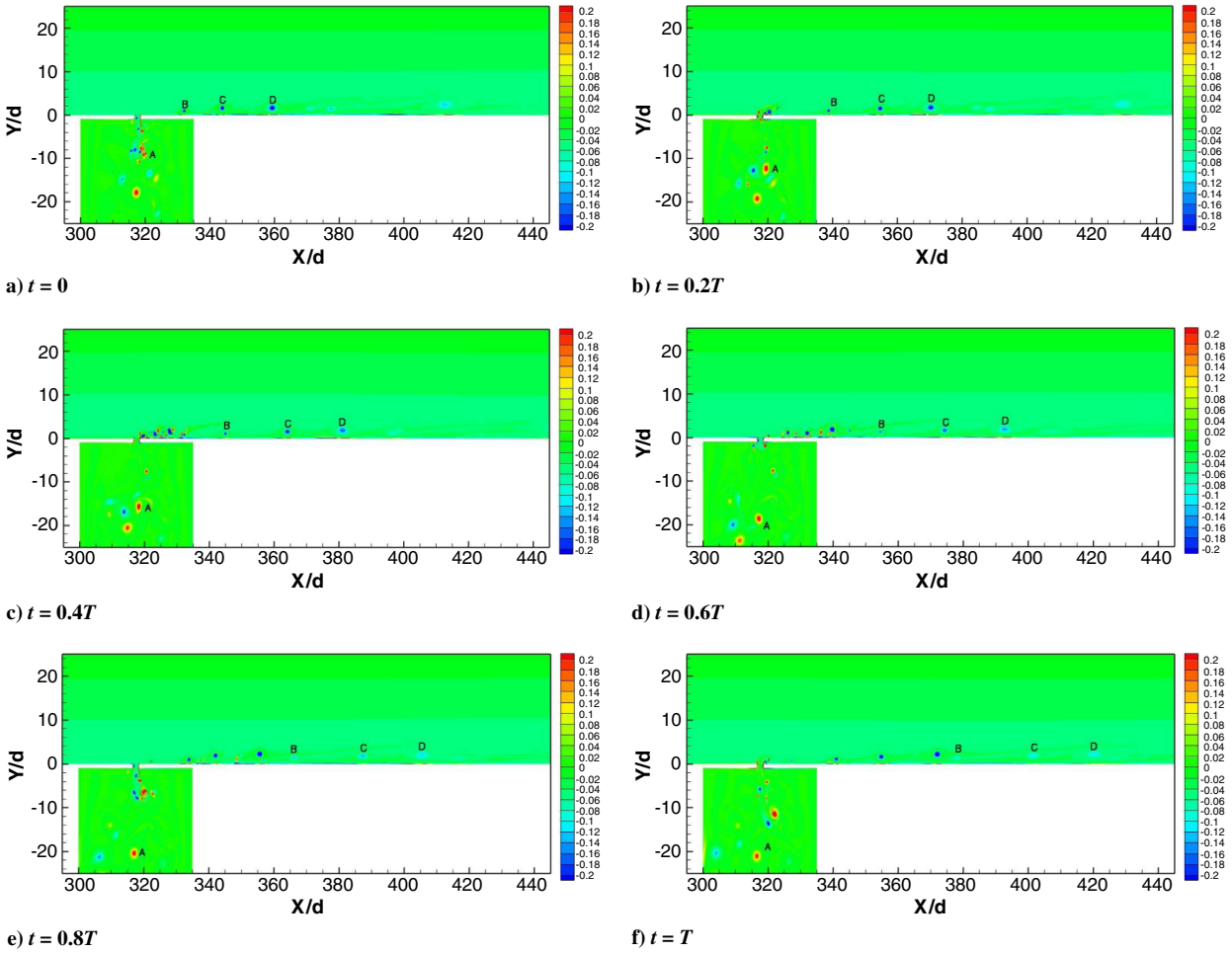

Fig. 8 Instantaneous vorticity contours $\zeta d/a_\infty$ of 150 dB incidence at 500 Hz in $M_\infty = 0.85$ grazing flow shown at 1/5th increments of the forcing period T.

upstream boundary, the subsonic inflow condition of [30], implemented in the form provided in [31], was used to enforce the boundary layer, while the upper and outflow boundaries used nonreflecting conditions. The upstream, downstream, and upper boundaries also used a sponge treatment to further enforce the grazing flow and prevent acoustic reflection [33]. All walls are isothermal, no-slip, and at temperature 300 K. The grid resolution within the boundary layer and near the aperture is critical and was checked by a grid-refinement study, for which the results are found in the Appendix. Approximately 200 points are located within the boundary layer, with the first grid point off the wall at a distance of less than one wall unit. The grid is finest within the aperture, with uniform spacing of size $\Delta x/D = \Delta y/D = 0.01$.

B. Impedance Prediction Method

The acoustic impedance is defined as the ratio of the acoustic pressure to the acoustic velocity at a point and is given by the complex number

$$Z = \frac{p^a}{v^a} = R + iX \tag{13}$$

where Z is the impedance value, p^a and v^a are acoustic pressure and acoustic velocity, respectively, and R and X are acoustic resistance and reactance, respectively. Frequently the impedance is normalized by the characteristic impedance of air $\rho_\infty a_\infty$ as

$$\frac{Z}{\rho_\infty a_\infty} = z = \theta + i\chi = \frac{R}{\rho_\infty a_\infty} + i\frac{X}{\rho_\infty a_\infty} \tag{14}$$

where z is the normalized impedance, and θ and χ are the normalized resistance and reactance, respectively.

There are several ways to determine the impedance of acoustic treatment panels experimentally, as discussed in [1]. We use the in situ two-microphone setup shown in Fig. 4, originally developed by Dean [5]. As noted in the figure, one sensor is mounted flush on the backplate of the cavity, while the other is inserted flush with the facesheet. The sensors' output are used to obtain the amplitude and relative phase of the two pressure signals. The normalized impedance for our SDOF liner is given by

$$z = -i\frac{\hat{p}_A}{\hat{p}_B}\frac{e^{i\phi}}{\sin(kH)} \tag{15}$$

where $\hat{p}_A$ and $\hat{p}_B$ are Fourier coefficients of the pressure signal, evaluated at the incident frequency, at the surface and backplate of the cavity, respectively, and ϕ is the phase difference between them. Also, H is the cavity depth and k is the wave number of the incident sound.

Applying Eq. (15) to the simulation results required the following procedure. From the original definition of acoustic impedance in Eq. (13) and its two-microphone application in Eq. (15), it is the acoustic pressure signal that is required. The presence of the grazing flow and the near-aperture vorticity field make it challenging to isolate the acoustic pressure from that associated with the hydrodynamic field near the aperture, so a point upstream of the aperture is used. Moreover, since the incident wave travels along the duct in the presence of a grazing flow, the pressure signals at different locations have different phases due to propagation that should be corrected before calculating the phase difference ϕ used in Eq. (15). Figure 7 provides a schematic of the phase correction at different locations, and the necessary correction formula is given by

$$\Delta\phi_i = \frac{d_i}{\lambda(1 + M_\infty)} \tag{16}$$

where d_i is the distance between the selected point facesheet measurement location A_i and the center point A of the aperture. The phase correction ϕ is then used in Eq. (15) as

$$\phi = \phi_{A_iB} - \Delta\phi_i \tag{17}$$

To assess the sensitivity of the predicted value of z to the facesheet probe location, as a function of grazing Mach number, four points

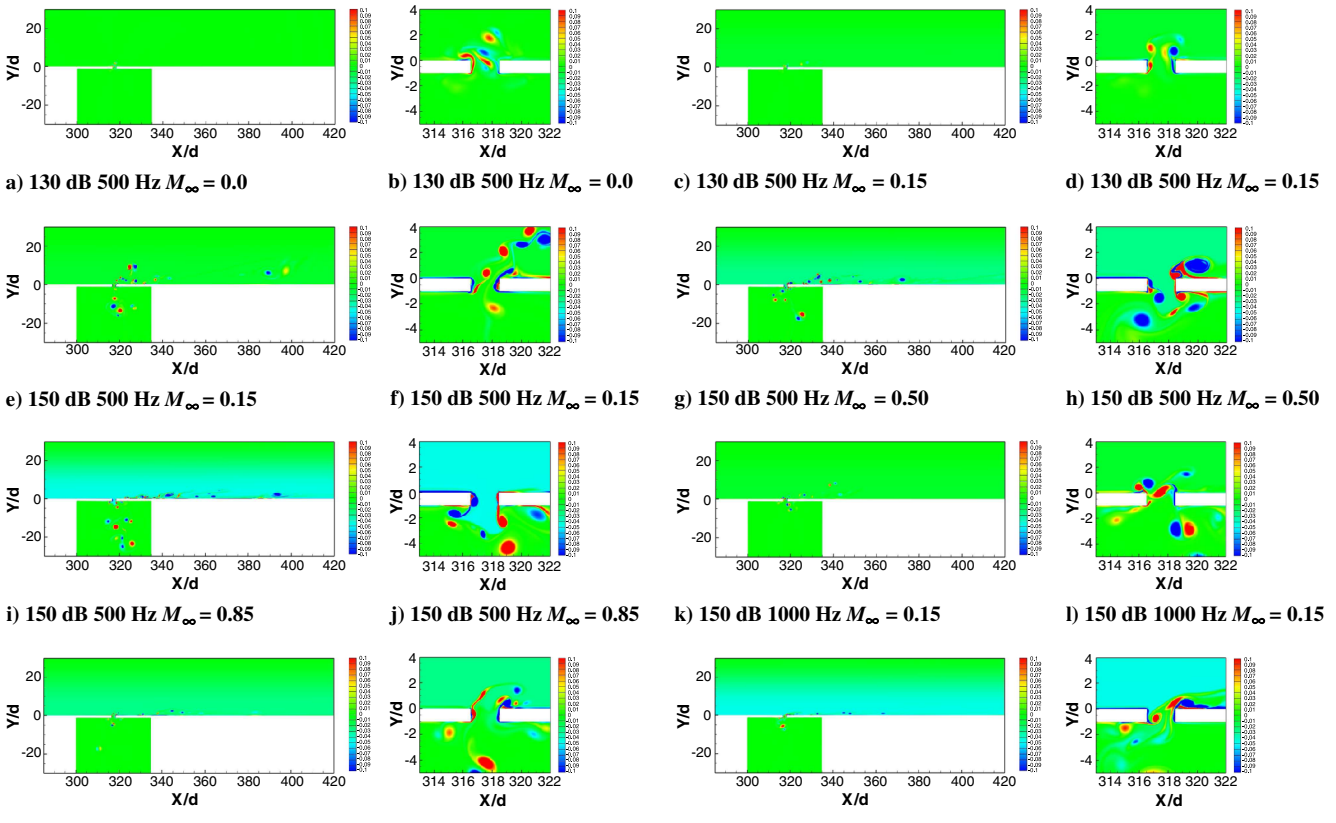

a) 130 dB 500 Hz $M_\infty = 0.0$ b) 130 dB 500 Hz $M_\infty = 0.0$ c) 130 dB 500 Hz $M_\infty = 0.15$ d) 130 dB 500 Hz $M_\infty = 0.15$

e) 150 dB 500 Hz $M_\infty = 0.15$ f) 150 dB 500 Hz $M_\infty = 0.15$ g) 150 dB 500 Hz $M_\infty = 0.50$ h) 150 dB 500 Hz $M_\infty = 0.50$

i) 150 dB 500 Hz $M_\infty = 0.85$ j) 150 dB 500 Hz $M_\infty = 0.85$ k) 150 dB 1000 Hz $M_\infty = 0.15$ l) 150 dB 1000 Hz $M_\infty = 0.15$

m) 150 dB 1000 Hz $M_\infty = 0.50$ n) 150 dB 1000 Hz $M_\infty = 0.50$ o) 150 dB 1000 Hz $M_\infty = 0.85$ p) 150 dB 1000 Hz $M_\infty = 0.85$

Fig. 9 Instantaneous vorticity contours $\zeta d/a_\infty$ of the simulation cases listed in Table 1.

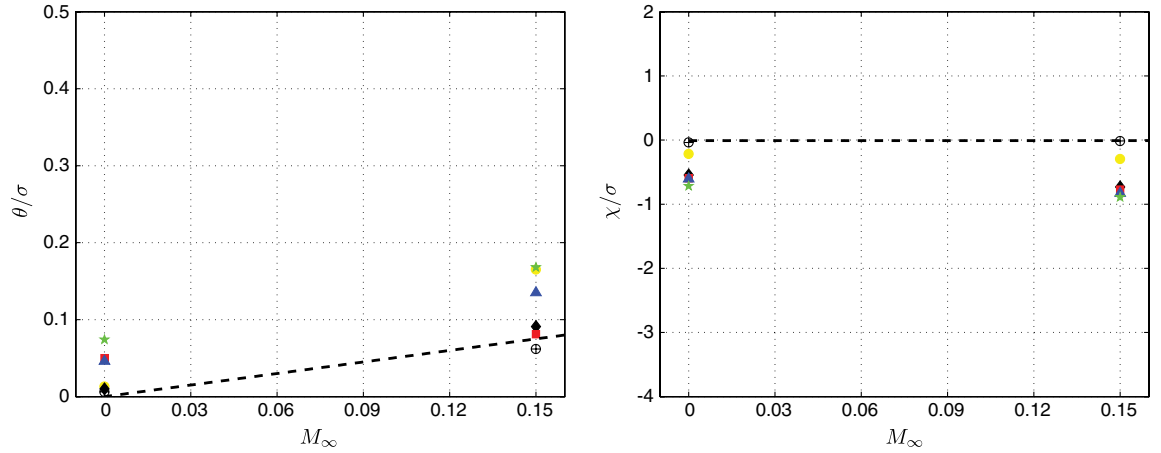

Fig. 10 Acoustic impedance prediction for 500 Hz, 130 dB incident sound, normalized by the porosity: resistance θ/σ (left) and reactance χ/σ (right) (dashed line: Rice [6] model; ⊕ : experimental data of Jing et al. [10]). Present numerical data using different facesheet locations (●: point A; ◆: point A_1; ■: point A_2; ▲: point A_3; ⋆: point A_4).

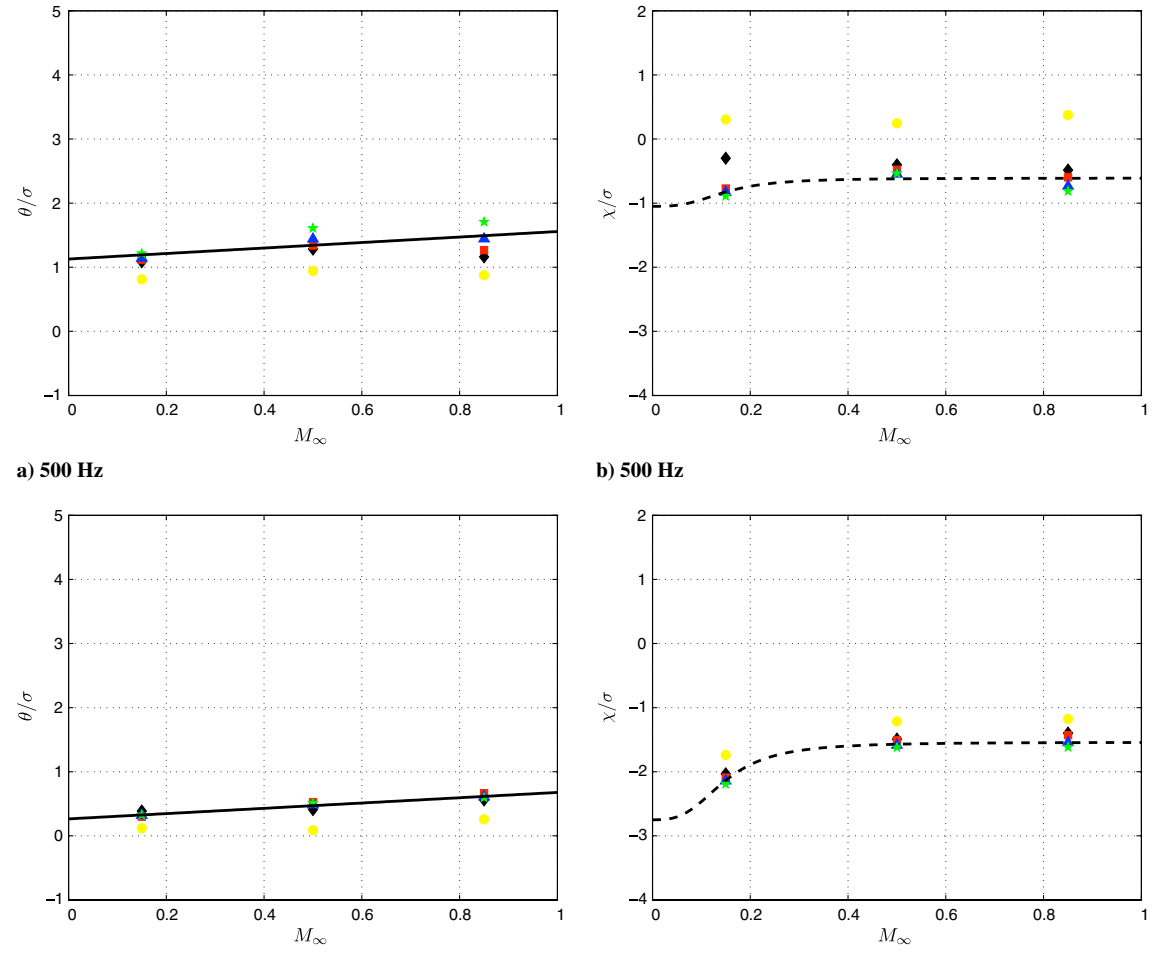

a) 500 Hz **b) 500 Hz**

c) 1000 Hz **d) 1000 Hz**

Fig. 11 Acoustic impedance prediction for 150 dB incident sound, normalized by the porosity, at 500 and 1000 Hz: resistance θ/σ (left column) and reactance χ/σ (right column) (solid and dashed lines) recalibrated model of Rice [6] model; present numerical data using different facesheet locations (●: point A; ◆: point A_1; ■: point A_2; ▲: point A_3; ⋆: point A_4).

upstream of the aperture and the center point of the aperture were selected for the impedance calculation and are listed in Table 2.

C. Flow Visualization

Figure 8 shows a time sequence of the instantaneous planar vorticity $\zeta = \partial v/\partial x - \partial u/\partial y$ for a 150 dB incidence with 500 Hz

Table 3 Curve fit coefficient resistance and reactance as a function of M_∞

Case	a	b	A	B	C
150 dB, 500 Hz	0.43	1.13	−0.61	−0.44	1.00
150 dB, 1000 Hz	0.41	0.26	−1.54	−1.21	1.00

frequency in a $M_\infty = 0.85$ grazing flow. For the first half cycle, when the duct pressure is higher than in the cavity, fluid is forced into the cavity through the aperture. Because of the sharp corners of the aperture, two large vortices are generated and followed by a series of smaller vortices. Half a cycle later, the pressure of the incident sound outside the resonator is lower and causes an outflow from the cavity to the duct through the aperture. For sufficiently large SPL, vorticity is shed from the aperture walls and convects downstream by the grazing flow. The present simulation agrees with the observation, of Tam et al. [23], that the vortices persist over a long distance downstream. Similar observations are found in other cases. Also note that different vortices migrate downstream with different velocity, depending on their height above the wall, as is visible in the vortices labeled B and C in Fig. 8.

Figure 9 shows global and near-aperture views of the vorticity field for all of the cases listed in Table 1, taken at the same relative phase of the incident sound. Note that the vortices generated by 130 dB incidence are weaker and confined to the aperture, while stronger vorticity is shed at 150 dB. A comparison between the images in Fig. 9 shows that more vorticity is shed at the lower frequency for a given amplitude, an observation also found in the no-flow case discussed in Sec. III. We note that the grazing flow also influences the shedding in that, instead of two sets of vortices generated and shed from the left and right neck boundaries, the vortices generated by the left wall quickly merge with the vortices generated by the right wall. Investigations of high subsonic cavity flows at much higher aperture-based Reynolds numbers have observed a similar merging process (Rowley et al. [35]).

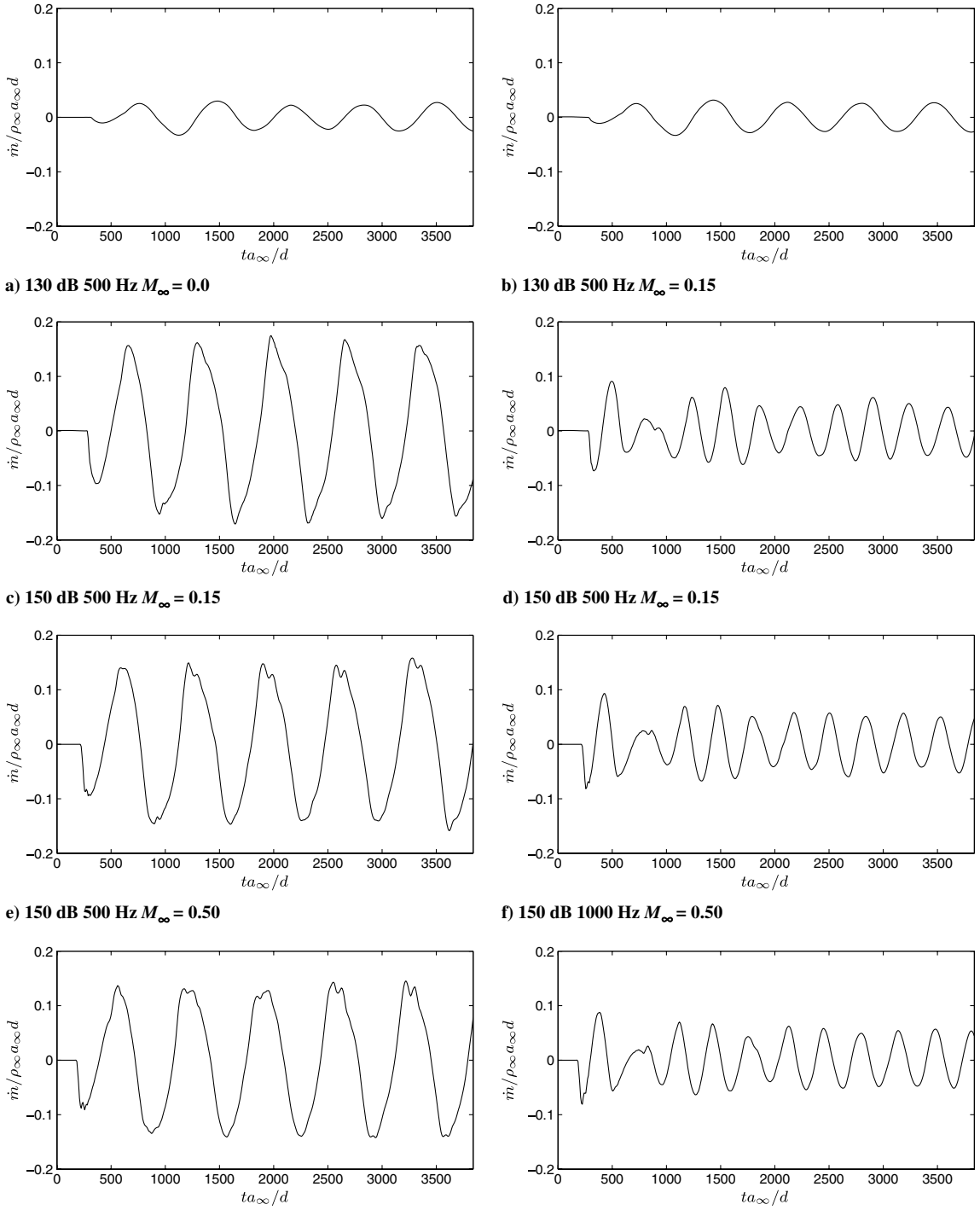

a) 130 dB 500 Hz $M_\infty = 0.0$

b) 130 dB 500 Hz $M_\infty = 0.15$

c) 150 dB 500 Hz $M_\infty = 0.15$

d) 150 dB 500 Hz $M_\infty = 0.15$

e) 150 dB 500 Hz $M_\infty = 0.50$

f) 150 dB 1000 Hz $M_\infty = 0.50$

g) 150 dB 1000 Hz $M_\infty = 0.85$

h) 150 dB 1000 Hz $M_\infty = 0.85$

Fig. 12 Mass flow rate of the numerical simulation cases listed in Table 1.

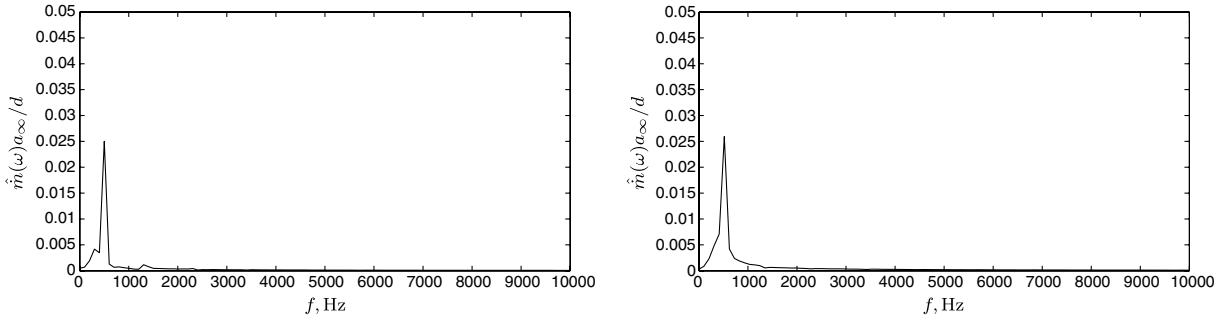

a) 130 dB 500 Hz $M_\infty = 0.0$ **b) 130 dB 500 Hz $M_\infty = 0.15$**

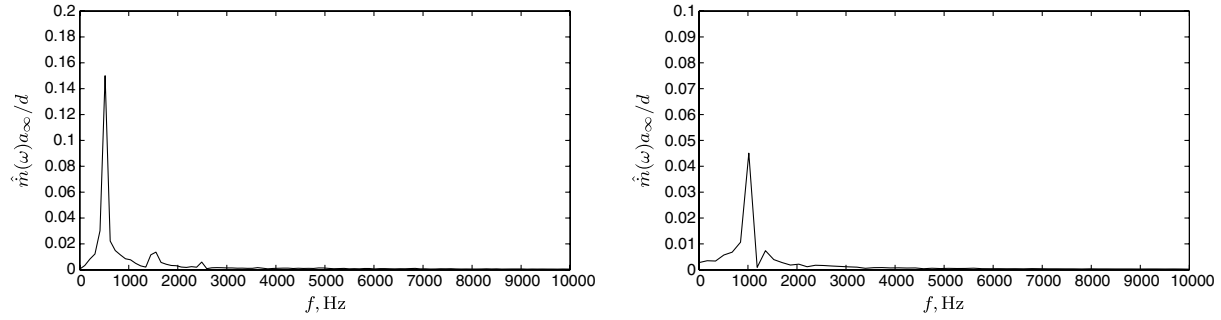

c) 150 dB 500 Hz $M_\infty = 0.15$ **d) 150 dB 500 Hz $M_\infty = 0.15$**

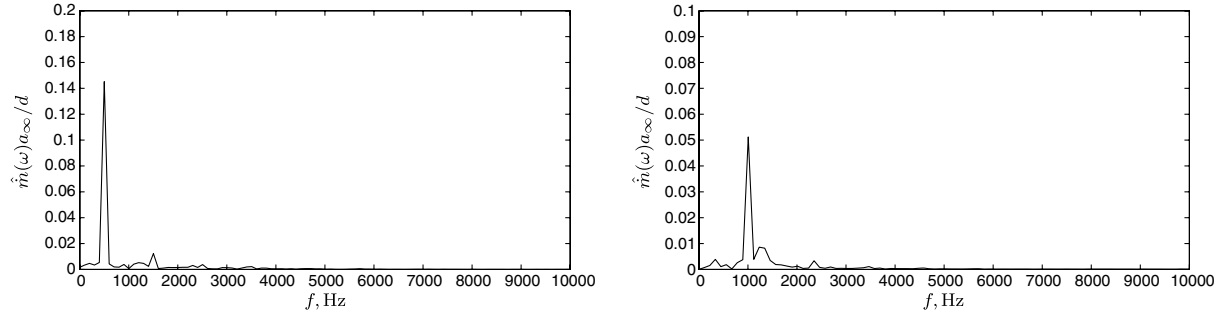

e) 150 dB 500 Hz $M_\infty = 0.50$ **f) 150 dB 1000 Hz $M_\infty = 0.50$**

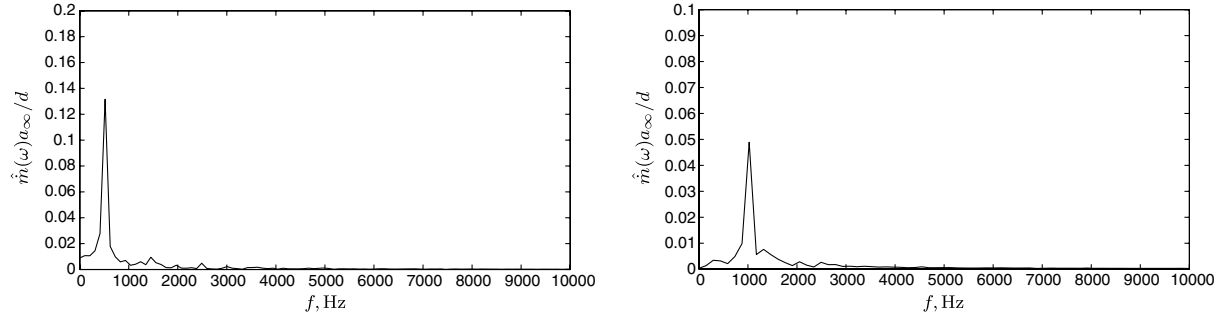

g) 150 dB 500 Hz $M_\infty = 0.85$ **h) 150 dB 1000 Hz $M_\infty = 0.85$**

Fig. 13 Spectra of mass flow rates corresponding to Fig. 12.

In high-speed grazing flow, once the vortices are ejected out of the cavity, they are immediately carried downstream. Nearly all the vortices are thus preferentially confined within the boundary layer. At lower speeds, the vortices have sufficient time to migrate farther vertically before being convected downstream and are thus found, on average, higher in the boundary layer.

D. Impedance Prediction

Figure 10 presents the acoustic impedance prediction, 130 dB incident sound using the simulation results, the experimental data of Jing et al. [10], and the semiempirical correlation of Rice [6]. In all cases, the impedance has been normalized by the porosity to permit

Table 4 Coefficients of curve fitting for mass flow rate

No	Case	A_0	ϕ_0
1	130 dB, 500 Hz, $M_\infty = 0.00$	0.025	1.86
2	130 dB, 500 Hz, $M_\infty = 0.15$	0.025	1.89
3	150 dB, 500 Hz, $M_\infty = 0.15$	0.155	2.70
4	150 dB, 500 Hz, $M_\infty = 0.50$	0.145	2.71
5	150 dB, 500 Hz, $M_\infty = 0.85$	0.137	2.71
6	150 dB, 1000 Hz, $M_\infty = 0.15$	0.048	1.42
7	150 dB, 1000 Hz, $M_\infty = 0.50$	0.051	1.39
8	150 dB, 1000 Hz, $M_\infty = 0.85$	0.050	1.51

comparison of the single-aperture simulations with multiaperture experiments and a semiempirical model. Note that, when there is no grazing flow, there is consistent agreement of the resistance values found for points A and A_1. The resistance predictions of points A_2, A_3, and A_4 differ, however. The scatter of the impedance values depending on the facesheet probe location is sizable and represents a significant uncertainty when predicting z from the simulation database. The variation in z with M_∞ is the same for all measurement points, with the aperture center location providing values close to that measured by Jing et al. [10], except for the resistance at $M_\infty = 0.15$.

These observations carry over to the higher grazing flow Mach number, 150 dB amplitude cases shown in Fig. 11. The simulation results show a linearly increasing resistance with M_∞ and a more complicated dependence for the reactance. The scatter of the predictions is still significant and increases with increasing M_∞, but we observe that, for facesheet points upstream of point A_1, there is relative agreement. Note that the trends of z using the aperture center point are not consistent with those found for the other measurement locations.

The data in Figs. 11a and 11c show that the resistance is a strong function of frequency and a relatively weak function of Mach number. There is less scatter in the impedance values (using the different facesheet measurement points) at lower Mach numbers and at higher frequencies. The latter observation is consistent with the visualizations in Figs. 8 and 9, where there was increased vortex shedding and, hence, increased perturbations of the near-aperture field, resulting in a larger hydrodynamic component to the pressure. The scatter in θ at 500 Hz is sufficient to preclude any conclusion regarding the variation of θ/σ with M_∞ valid for all points. Instead, for the face sheet measurement point farthest away from the aperture, there is a monotonic increase of θ/σ with M_∞, while closer measurement locations level off, or decrease, as M_∞ increases.

To put these values into the context of existing liner models, we use the semiempirical result [1] that the porosity-normalized characteristic resistance and reactance values scale with M_∞ as $\theta/\sigma = aM_\infty + b$ and $\chi/\sigma = A + B/(1 + CM_\infty^3)$, respectively, in lieu of experimental data. (There do not appear to be experimental data of slit liners at high values of M_∞.) The original fits were calibrated using circular aperture liners, and we do not expect the resulting coefficients to apply to our slit liner; however, the trends with M_∞ represent physical processes that are present in the simulation data. Fitting the data to these two expressions results in the parameters found in Table 3 and provides preliminary justification, at least for the 1 kHz case, for their use at high grazing flow Mach numbers.

V. Time-Domain Liner Quantities

In this section, the simulation databases, which have been shown to be consistent with previous no-flow and low-velocity flow liner data, and with semiempirical modeling expectations at high grazing flow Mach numbers, are examined in the context of time-domain liner models, such as the one proposed by Hersh et al. [27]. The success, and eventual adoption, of time-domain liner models is still being assessed. Multifrequency phenomena, including high-amplitude tonal sound or turbulent pressure fluctuations, are more naturally represented in the time domain, but a reliable model linking the absorption of sound by a liner has not been developed. It has been shown by Tam and Auriault [36] that one cannot take a frequency domain model and convert it into the time domain without an analysis of well posedness. The model in [27], which shares some similarities to the one developed by Eldredge and Dowling [13], attempts to use a control volume formulation to relate the acceleration of the fluid through the aperture to the pressure difference across it, while including wall viscous losses due to oscillatory boundary layers and inertia effects. In part because of a lack of data, Hersh et al. [27] simplify their time-domain model into a single frequency model. The results of this section are an attempt to provide the necessary time-domain data to make such a multifrequency model feasible. The reader is referred to the original work by Hersh et al. for the model's derivation and the origin of the terms we present.

A. Mass Flow Rate Distribution

The first term to be examined is the time-dependent mass flow rate, given by

$$\dot{m}(t) = \int_0^D \rho(t) v(t)\, \mathrm{d}x \tag{18}$$

where the integration extends over the entire liner aperture. In Fig. 12, it is seen that the mass flow rate is a function of both the incidence SPL and the incidence frequency. After the transition period, time-periodic, but not necessarily single frequency, states are found in all the simulation results. The steady-state amplitude of the mass flow rate is higher for larger SPL, as is to be expected. Second, for the lower SPL cases, the mass flow rates are nearly sinusoidal after the transition period, while for higher SPL cases, especially those at lower frequencies, the mass flow rates tend to have nonlinear behavior, and secondary peaks are found in Figs. 12e and 12g.

These results are further quantified in Fig. 13, which show the Fourier transform of the statistically stationary mass flow rate in the frequency domain. A single dominant peak is found in all cases and is nearly equal to the corresponding incidence frequency. Minor harmonic conduct is detected for 150 dB amplitude. These results suggest that a simple a cosine curve fit can be used to model $\dot{m}$, as

$$\dot{m} = A_0 \cos[2\pi f(t - t^\dagger) + \phi_0] \tag{19}$$

where f is the incident frequency, $t^\dagger$ is the retarded time with respect to a convenient reference, and the coefficients A_0, ϕ_0 can be determined from a fast Fourier transform . We choose to split $t^\dagger$ from ϕ_0, because the phase change due to propagation may be a separate input in application of the model. Table 4 tabulates the coefficients in

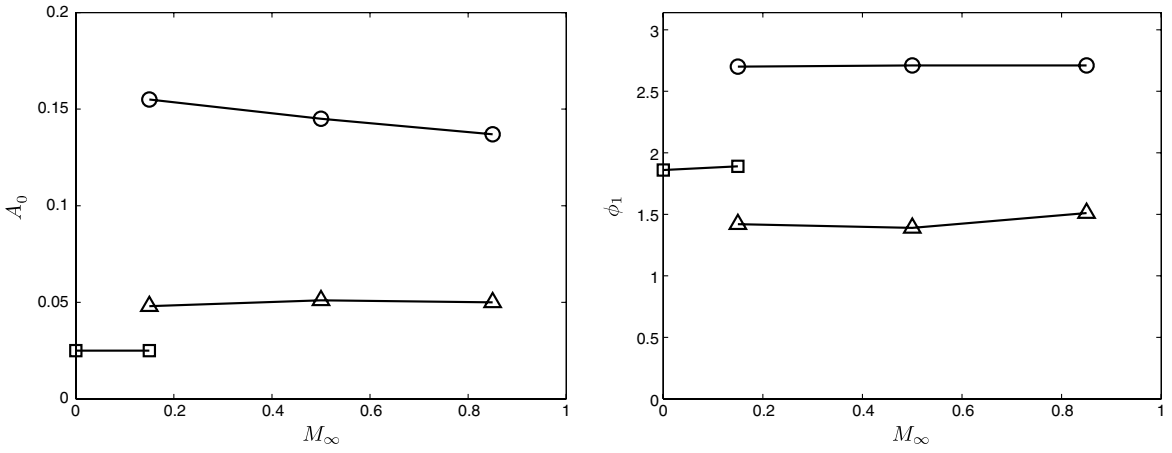

Fig. 14 Parametric dependence of mass flow rate curve fit (□: 130 dB, 500 Hz; ○: 150 dB, 500 Hz; △: 150 dB, 1000 Hz).

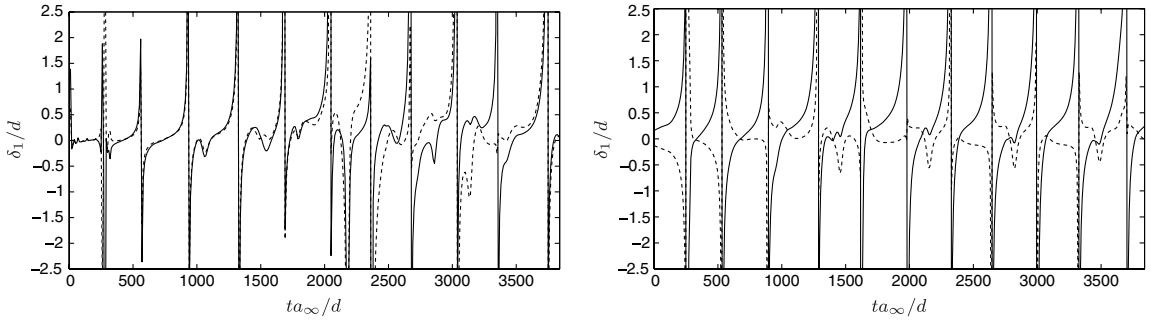

a) 130 dB 500 Hz $M_\infty = 0.0$ **b) 130 dB 500 Hz $M_\infty = 0.15$**

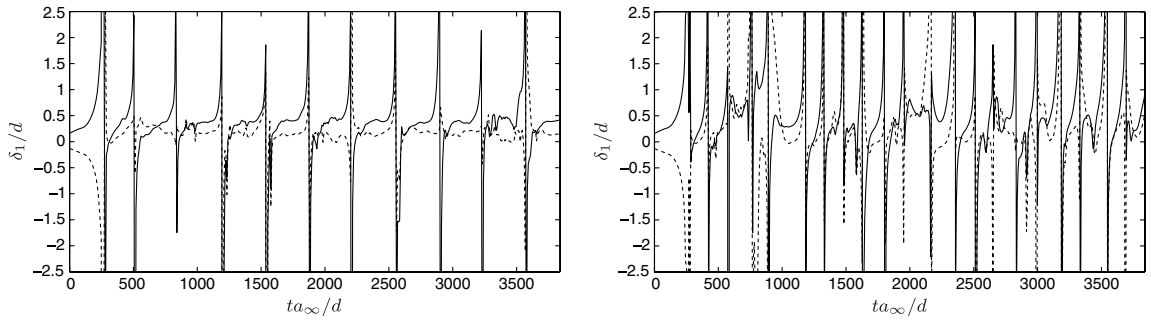

c) 150 dB 500 Hz $M_\infty = 0.15$ **d) 150 dB 500 Hz $M_\infty = 0.15$**

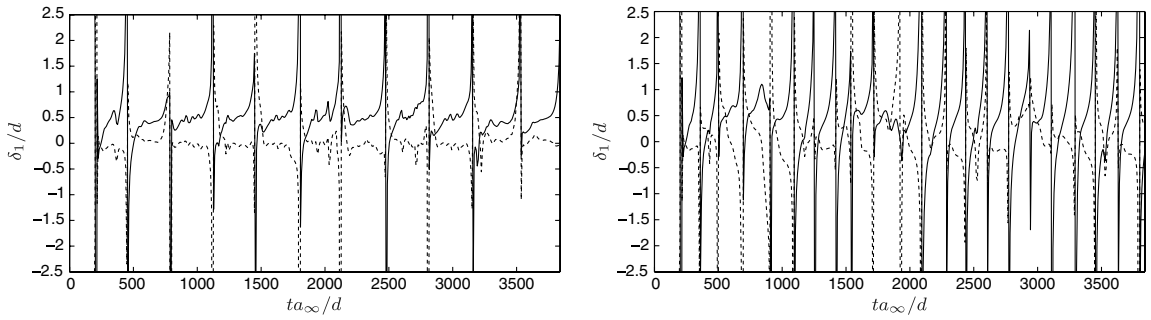

e) 150 dB 500 Hz $M_\infty = 0.50$ **f) 150 dB 1000 Hz $M_\infty = 0.50$**

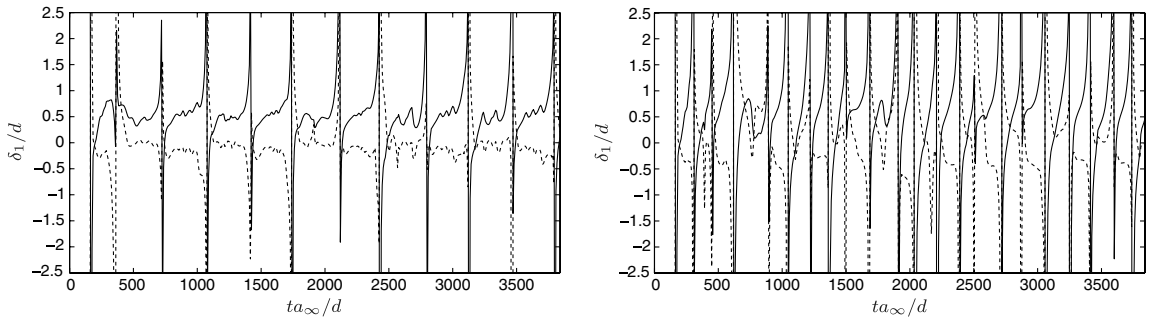

g) 150 dB 1000 Hz $M_\infty = 0.85$ **h) 150 dB 1000 Hz $M_\infty = 0.85$**

Fig. 15 Aperture wall displacement thickness distribution (solid line: left wall; dashed line: right wall).

Eq. (19), while Fig. 14 shows the variation of these parameters with the flow conditions. A tiny decrease of A_0 is found in 150 dB, 500 Hz cases when M_∞ increases but, on the whole, A_0 is rather insensitive to the change of M_∞.

B. Displacement Thickness Distribution

The vorticity field discussed earlier revealed a significant boundary-layer character in the aperture region, and the time-domain model of Hersh et al. [27] uses a discharge coefficient to model the boundary-layer effect on the flux through the aperture. Here, we present the displacement thickness on the aperture walls directly. Because of the presence of the grazing flow, it is necessary to study the displacement thickness on both neck walls. By traditional definition of displacement thickness, we define

$$\delta_{1L} = \int_0^{\frac{D}{2}} \left[1 - \frac{\rho(x,t)v(x,t)}{[\rho(t)v(t)]_{\text{ref}}}\right] \mathrm{d}x \tag{20}$$

$$\delta_{1R} = \int_{\frac{D}{2}}^{D} \left[1 - \frac{\rho(x,t)v(x,t)}{[\rho(t)v(t)]_{\text{ref}}}\right] \mathrm{d}x \tag{21}$$

where δ_{1L} and δ_R denote the left and right displacement thickness, respectively, and $[\rho(t)v(t)]_{\text{ref}}$ is evaluated at a reference position, chosen here to be at the centerline of the aperture.

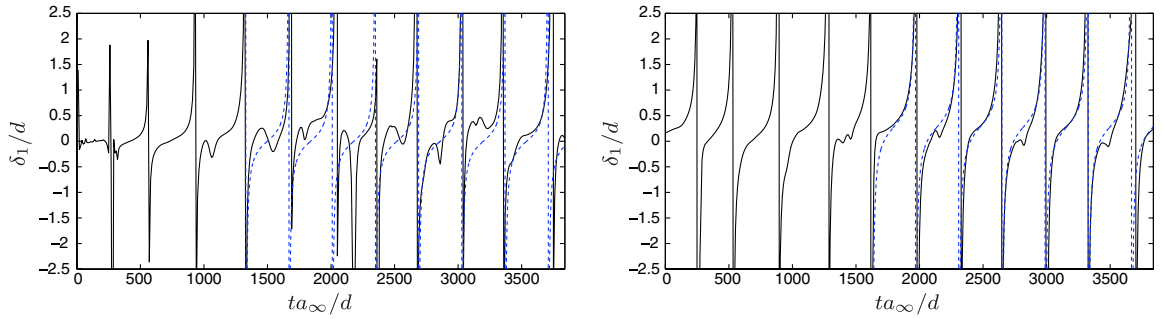

a) 130 dB 500 Hz $M_\infty = 0.0$

b) 130 dB 500 Hz $M_\infty = 0.15$

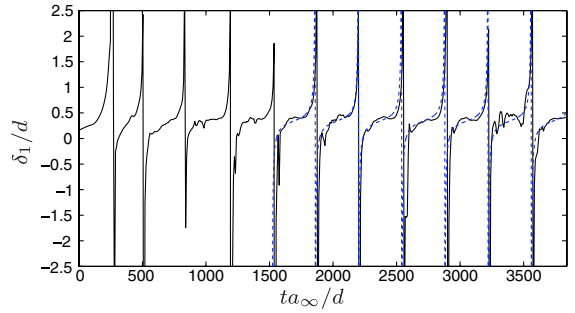

c) 150 dB 500 Hz $M_\infty = 0.15$

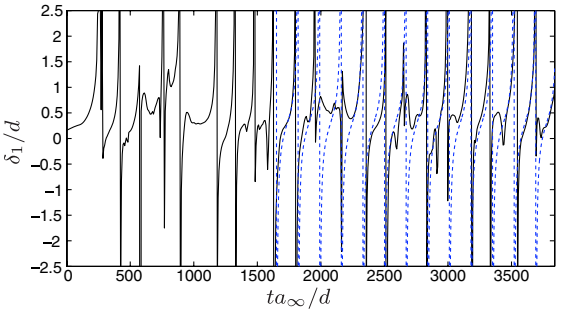

d) 150 dB 500 Hz $M_\infty = 0.15$

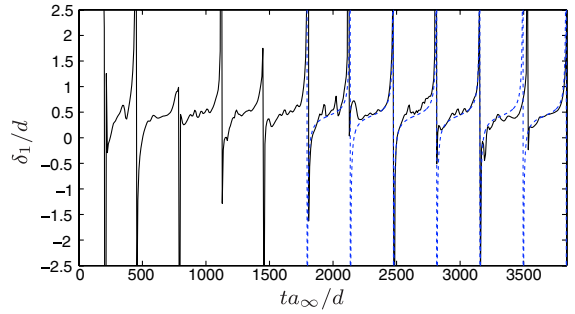

e) 150 dB 500 Hz $M_\infty = 0.50$

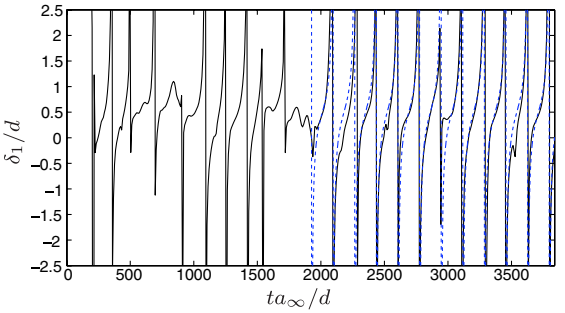

f) 150 dB 1000 Hz $M_\infty = 0.50$

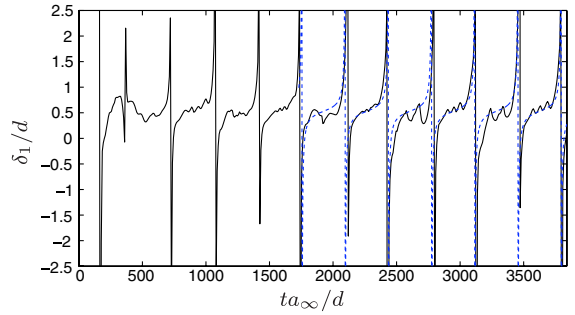

g) 150 dB 1000 Hz $M_\infty = 0.85$

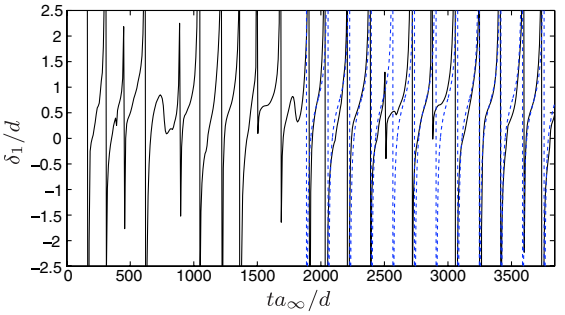

h) 150 dB 1000 Hz $M_\infty = 0.85$

Fig. 16 Analytical fit of upstream aperture wall displacement thickness (solid line: simulation data; dashed line: curve fit).

Figure 15 shows that the left and right displacement thicknesses can be quite different, and this difference is closely related to the freestream Mach number because of the presence of the grazing flow. Also note that the displacement thickness distributions, especially the right displacement thickness, behave differently between the first half cycle and the second half cycle. The integral in Eqs. (20) and (21) diverges when $v_{\text{ref}} \to 0$, which forms clear boundaries for the half cycles of the flowfield. In Figs. 16a and 16b, for 130 dB incident waves, for the first half cycle when pressure outside the cavity is higher than the pressure inside the cavity, the left displacement thickness tends to grow, although a decrease may be found in some small intervals until the reference velocity goes to zero. No significant difference is found for the left displacement thickness

Table 5 Coefficients of curve fitting for left displacement thickness

No.	Case	A_1	ϕ_1	δ_0
1	130 dB, 500 Hz, $M_\infty = 0.00$	0.29	−1.57	0.03
2	130 dB, 500 Hz, $M_\infty = 0.15$	0.32	−1.53	0.28
3	150 dB, 500 Hz, $M_\infty = 0.15$	0.11	−0.52	0.34
4	150 dB, 500 H,z $M_\infty = 0.50$	0.12	−0.53	0.43
5	150 dB, 500 Hz, $M_\infty = 0.85$	0.11	−0.52	0.53
6	150 dB, 1000 Hz, $M_\infty = 0.15$	0.44	−1.87	0.31
7	150 dB, 1000 Hz, $M_\infty = 0.50$	0.46	−1.85	0.49
8	150 dB, 1000 Hz, $M_\infty = 0.85$	0.47	−1.81	0.71

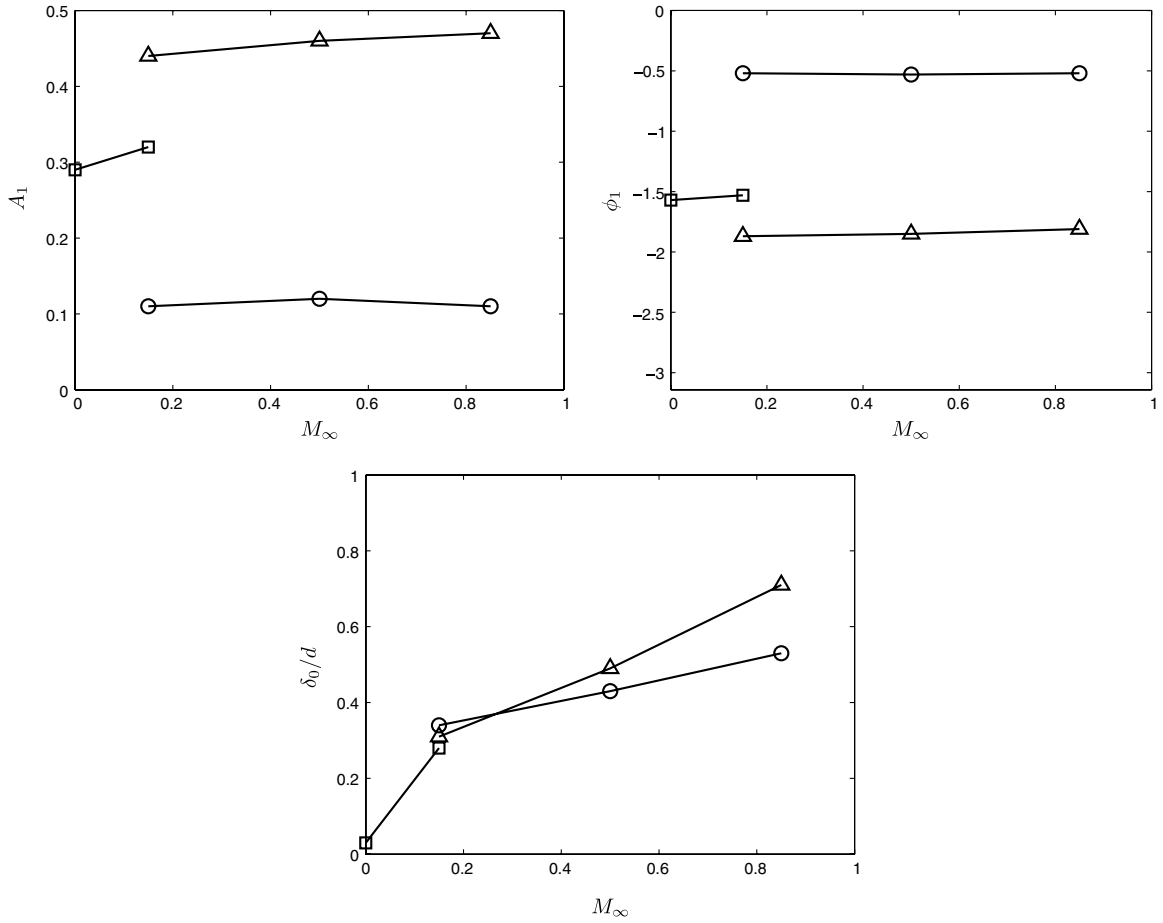

Fig. 17 Parametric dependence of upstream aperture wall curve fit (□: 130 dB, 500 Hz; ◯: 150 dB, 500 Hz; △: 150 dB, 1000 Hz).

distribution for the second half cycle. However, with the presence of the grazing flow, Fig. 16b reveals an obvious trough for the right displacement thickness distribution. Both the left and right boundary layers develop a clean periodic behavior after several periods.

Figure 16a shows symmetric response to the grazing incident wave in the absence of flow. At this condition, the excited flowfield is statistically symmetric, and the vortices are being generated at the same amount by these two boundaries. The phase difference in the incident sound between the left and right boundaries is small, since the aperture size is much smaller than the wavelength. Because the shed shear layers are Kelvin–Helmholtz unstable and vortex patterns are no longer symmetric (see Fig. 9b), the left and right displacement thicknesses may be slightly different for a particular cycle but statistically similar over many periods.

For 150 dB incident waves, the displacement thickness response is more complicated. As noted in Figs. 16c, 16e, and 16g, the right displacement thickness is near zero, except for the flow reversal regions. This phenomenon was not observed in Figs. 16c, 16e, and 16g. Also note in these figures that significant short time-scale disturbances emerge in both of the left and right displacement thickness distributions caused by the passage of discrete vorticity through the aperture.

It is interesting to point out that the left (i.e., upstream) displacement thickness is qualitatively similar to the trigonometric tangent function in each cycle. On this observation, curve fits of the form

$$\delta_{1L} = A_1 \tan[2\pi f(t - t^\dagger) + \phi_1] + \delta_0$$

are applied to the left displacement thickness, with coefficients tabulated in Table 5. Variation of the parameter with M_∞, f, and SPL is shown in Fig. 17. A_1 and ϕ_1 are mostly a function of the SPL and frequency f only. Also note that when the frequency and SPL of incidence are fixed, a linear increase of Mach number M_∞ will result in a linear increase of δ_0. No useful fit was found for the right, downstream, displacement thickness, except that, as M_∞ increased, the data suggest that $\delta_{1R} \approx 0$ for most of the cycle.

C. Wall Shear Stress Distribution

The final time-domain quantity to be considered is the wall shear stress along the aperture neck, defined here as

$$\tau_L = \frac{1}{Re}\int_0^d \mu \frac{\partial v}{\partial x}\bigg|_{\text{left wall}} \mathrm{d}y \tag{22}$$

$$\tau_R = \frac{1}{Re}\int_0^d \mu \frac{\partial v}{\partial x}\bigg|_{\text{right wall}} \mathrm{d}y \tag{23}$$

where τ_L and τ_R denote left and right wall shear stresses, respectively, and d is the thickness of the perforated sheet plate.

Figure 18 provides the wall shear stress distribution in time domain. It can be directly observed that lower wall shear stress fluctuations are found in the 130 dB cases. For all of the cases using 150 dB incident waves, higher amplitudes of the wall shear stress are observed in the lower frequency (500 Hz) cases with significant aperiodicity. The spectral content of τ_L and τ_R are presented in Fig. 19. A comparison between Figs. 19b and 19c shows lower wall shear stresses are found at lower SPL conditions. Also note that, in Figs. 19d, 19f, and 19h, there is always a difference between the left and right shear stress strengths, and this difference is increased when the grazing flow Mach number is increased. Symmetry of the wall shear stress is achieved in the case when there is no grazing flow in the duct (see Fig. 19a).

In considering the spectra of the wall shear stress, Fig. 19d shows that for 1000 Hz cases, the spectra have an obvious peak around 1000 Hz. However, for all 500 Hz cases, it is observed that more than

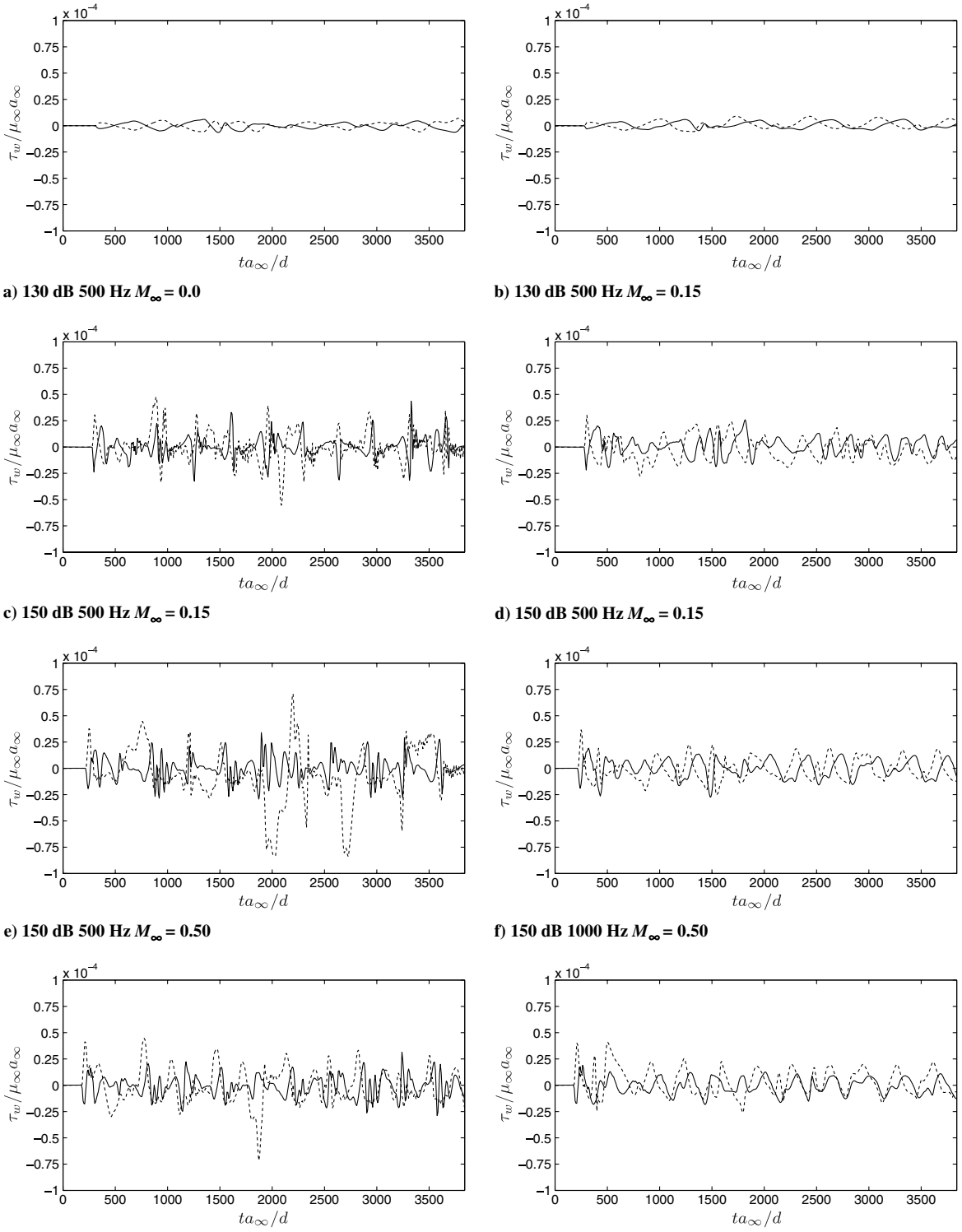

a) 130 dB 500 Hz $M_\infty = 0.0$ **b) 130 dB 500 Hz $M_\infty = 0.15$**

c) 150 dB 500 Hz $M_\infty = 0.15$ **d) 150 dB 500 Hz $M_\infty = 0.15$**

e) 150 dB 500 Hz $M_\infty = 0.50$ **f) 150 dB 1000 Hz $M_\infty = 0.50$**

g) 150 dB 1000 Hz $M_\infty = 0.85$ **h) 150 dB 1000 Hz $M_\infty = 0.85$**

Fig. 18 Aperture wall shear stress distribution (solid line: left wall; dashed line: right wall).

one spectral peak exists, the higher frequency of which are related to the fact that the 500 Hz incidence case is more capable of vortex shedding and these vortices perturb the wall shear stress as they pass through the aperture. The individual cycle variation of τ_w is significant, so phase-averaged results are shown in Fig. 20. It is noted that all the 130 dB cases and 150 dB, 1000 Hz cases have a good fit between the raw and phase-averaged fit data in both the left and right wall shear stresses, whereas the 150 dB, 500 Hz case does not, indicating the role of the vortex shedding.

When combined, these results suggest that a time-domain wall shear stress model may be difficult to construct, which demonstrates the correct variation with flow and sound properties, especially over a wide frequency range. It is to be emphasized, however, that these results are for a slit liner and may not be consistent for 3-D liners with circular apertures.

VI. Conclusions

In this work, numerical simulations were performed for incident waves with different intensities and frequencies, as well as with different grazing flow Mach numbers, to investigate the response of slit liners and their impedance properties. As with previous

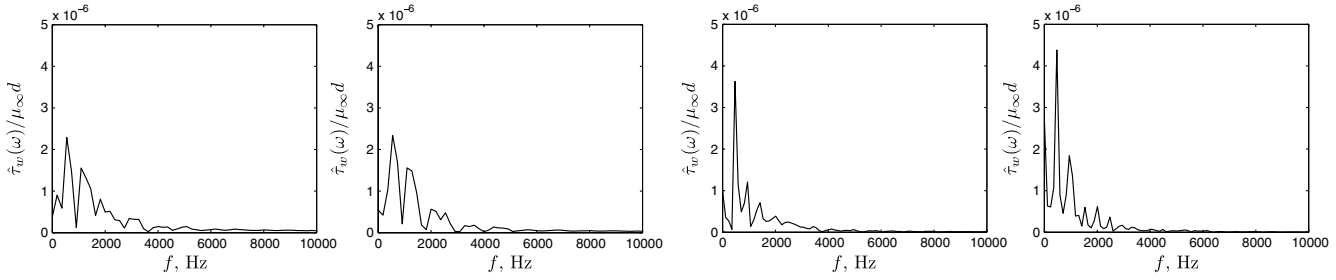

a) 130 dB 500 Hz $M_\infty = 0.0$ **b) 130 dB 500 Hz $M_\infty = 0.15$**

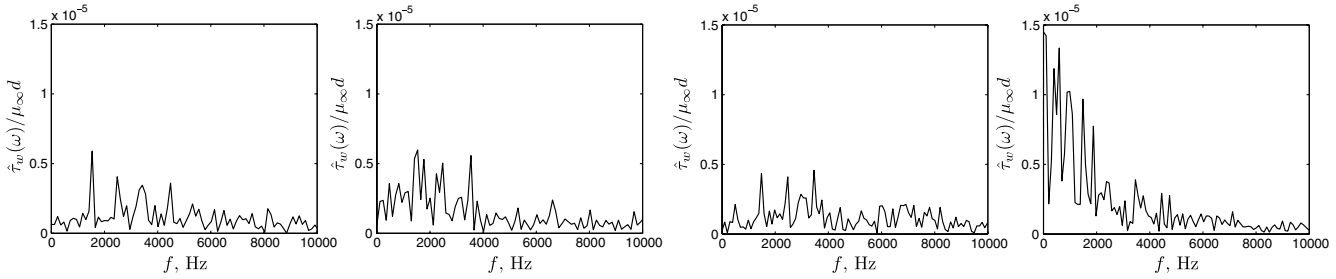

c) 150 dB 500 Hz $M_\infty = 0.15$ **d) 150 dB 500 Hz $M_\infty = 0.50$**

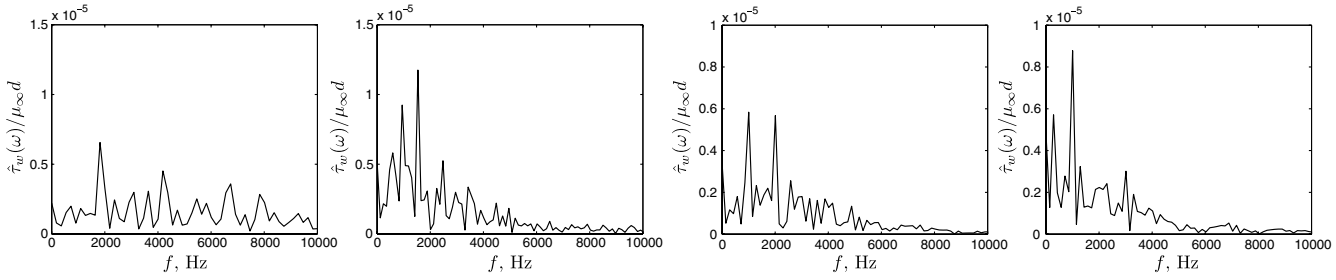

e) 150 dB 500 Hz $M_\infty = 0.85$ **f) 150 dB 1000 Hz $M_\infty = 0.15$**

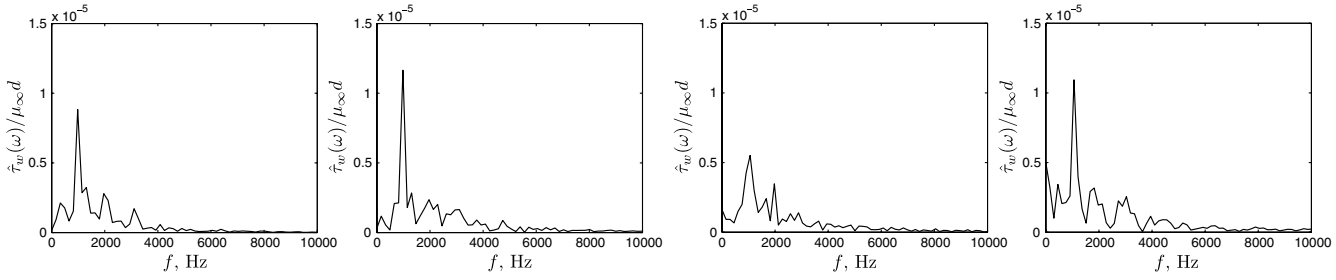

g) 150 dB 1000 Hz $M_\infty = 0.50$ **h) 150 dB 1000 Hz $M_\infty = 0.85$**

Fig. 19 Spectra of mass flow rates corresponding to Fig. 18: left wall (left column) and right wall (right column).

investigations, vortex generation and shedding were found near the liner aperture. For high Mach number grazing flow, the shed vortices are typically found lower in the boundary layer, whereas for low Mach number grazing flow, the shed vortices are able to penetrate into higher portions of the boundary layer. It is reasonable to infer in the former case that these vortices may have an impact on their neighboring liner, depending on the distance of two apertures. The impedance was evaluated through the viewpoint of the traditional two-microphone method and compared with experimental data and to semiempirical models. Reasonable agreement was found between the experimental data for most of the lower SPL and lower Mach number cases. Existing semiempirical correlations of the impedance with Mach numbers $\sigma \propto M_\infty$ and $\chi \propto 1/(1 + aM_\infty^3)$ appear consistent with the current data. Scatter was observed in the predicted impedance, which increased with increasing Mach number.

Several time-domain model quantities proposed in the literature were examined using the simulation databases. The time-dependent aperture mass flux, boundary-layer thickness, and wall shear were examined and correlated with the grazing flow and incident sound properties. At high grazing flow Mach numbers, the boundary-layer asymmetry becomes significant, an effect that should be included in future models. It was also found that the mass flux and displacement thickness could be effectively modeled with analytical functions for which the temporal dependence was imposed by the incident sound. For the wall shear stress, however, this was not the case with significant per-cycle variation and frequencies other than that of the incident sound. A suitable analytical function was not found.

Appendix

An evaluation of the grid used for the grazing flow studies was conducted to assess whether the measured impedance was accurately captured. Two grids were considered: our production grid of size 1301×1201 in the x and y directions, respectively, with minimum spacing of $0.01D$ and a coarser mesh of size 651×601, with minimum spacing $0.02D$. The domain sizes were identical (see Fig. 6), and the same boundary conditions and time steps were used; only the grid spacing was changed. The physical parameters were

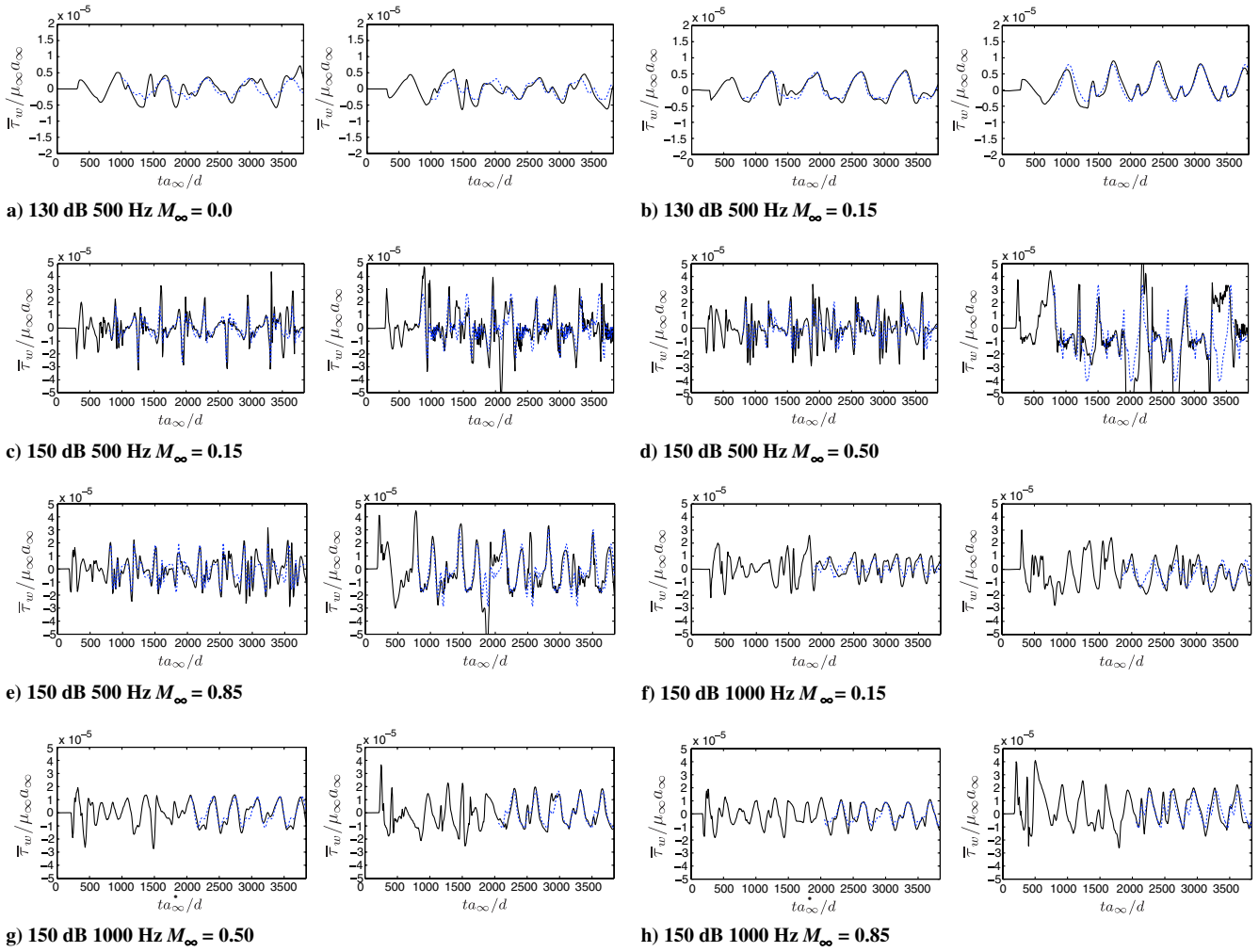

Fig. 20 Wall shear stress phase average: left wall (left column) and right wall (right column) (solid line: instantaneous data; dashed line: phase-averaged results).

$M_\infty = 0.50$, frequency 1 kHz, and 150 dB amplitude. The results, as summarized in Fig. A1 for the pressure and vertical velocity, show that there is substantial agreement at the center of the aperture for all times, with agreement in amplitude and phase when the flow becomes statistically stationary. The difference in the impedance between the two data sets is 5% for both the resistance and reactance. The data in Fig. A1 represent the worst agreement found between the two simulations and demonstrate that our impedance predictions are grid independent.

Acknowledgments

This work was supported by the AeroAcoustics Research Consortium and NASA Supersonic Program (award no. NNX07AC94A; J. Debonis and J. Bridges are the technical monitors). Computational resources from the Turing Cluster, operated by the Computational Science and Engineering Department, University of Illinois at Urbana-Champaign, are greatly acknowledged.

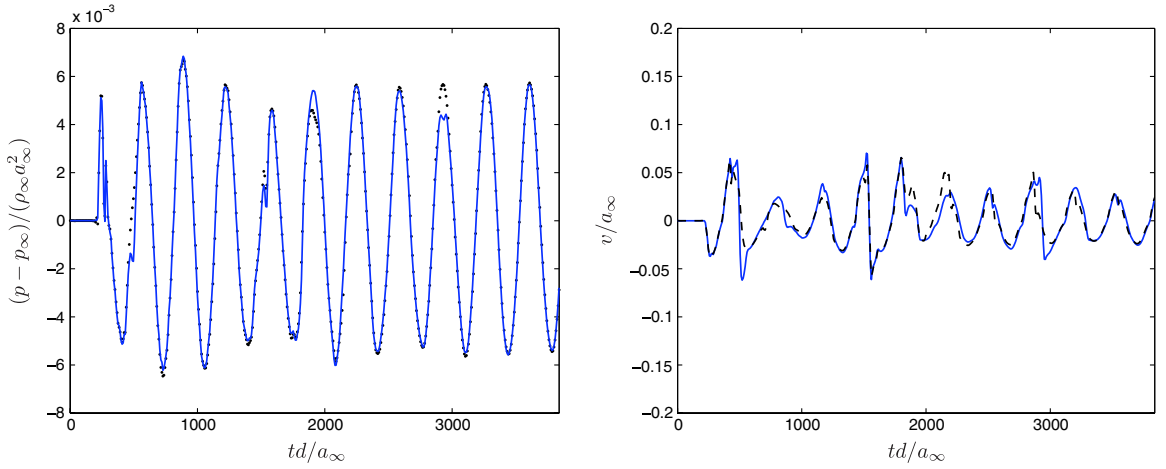

Fig. A1 Grid refinement study for Mach 0.50 grazing flow case at 1 kHz and 150 dB. The pressure (left) and vertical velocity (right) are shown in the center of the liner aperture for coarse (dashed line) and fine (solid line) meshes.

References

[1] Motsinger, R. E., and Kraft, R. E., *Design and Performance of Duct Acoustic Treatment: Aeroacoustics of Flight Vehicles, Volume 2 of Noise Control*, NASA, Aug. 1991.

[2] Ingard, U., and Labate, S., "Acoustic Circulation Effects and the Nonlinear Impedance Of Orifices," *Journal of the Acoustical Society of America*, Vol. 22, No. 2, Aug. 1950, pp. 211–219. doi:10.1121/1.1906591

[3] Melling, T. H., "The Acoustic Impedance of Perforates at Medium and High Sound Pressure Levels," *Journal of Sound and Vibration*, Vol. 29, No. 1, Aug. 1973, pp. 1–65. doi:10.1016/S0022-460X(73)80125-7

[4] Hersh, A. S., and Rogers, T., "Fluid Mechanical Model of the Acoustic Impedance of Small Orifices," AIAA, New York, March 1975, pp. 75–495.

[5] Dean, P. D., "In Situ Method of Wall Acoustic Impedance Measurement in Flow Ducts," *Journal of Sound and Vibration*, Vol. 34, No. 1, 1974, pp. 97–130. doi:10.1016/S0022-460X(74)80357-3

[6] Rice, E. J., "Theoretical Study of the Acoustic Impedance of Orifices in the Presence of a Steady Grazing Flow," *Journal of the Acoustical Society of America*, Vol. 59, April 1976, pp. S32–S32. doi:10.1121/1.2002637

[7] Howe, M. S., "On the Theory of Unsteady High Reynolds Number Flow Through a Circular Aperture," *Proceedings of the Royal Society of London A*, Vol. 366, No. 1725, 1979, pp. 205–223. doi:10.1098/rspa.1979.0048

[8] Zorumski, W. E., and Tester, B. J., "Prediction of the Acoustic Impedance of Duct Liners," NASA Langley Research Center TM X-73951, Hampton, VA, 1979.

[9] Jing, X., and Sun, X., "Experimental Investigations of Perforated Liners with Bias Flow," *Journal of the Acoustical Society of America*, Vol. 106, No. 5, 1999, pp. 2436-2441. doi:10.1121/1.428128

[10] Jing, X., Sun, X., Wu, J., and Meng, K., "Effect of Grazing Flow on the Acoustic Impedance of an Orifice," *AIAA Journal*, Vol. 39, No. 8, Aug. 2001, pp. 1478–1484. doi:10.2514/2.1498

[11] Hughes, I. J., and Dowling, A. P., "The Absorption of Sound by Perforated Linings," *Journal of Fluid Mechanics*, Vol. 218, 1990, pp. 299–335. doi:10.1017/S002211209000101X

[12] Dowling, A. P., and Hughes, I. J., "Sound Absorption by a Screen with a Regular Array of Slits," *Journal of Sound and Vibration*, Vol. 156, No. 3, 1992, pp. 387–405. doi:10.1016/0022-460X(92)90735-G

[13] Eldredge, J. D., and Dowling, A. P., "The Absorption of Axial Acoustic Waves by a Perforated Liner with Bias Flow," *Journal of Fluid Mechanics*, Vol. 485, Jan. 2003, pp. 307–335. doi:10.1017/S0022112003004518

[14] Cummings, A., "A Finite Element Scheme for Acoustic Transmission Through the Walls of Rectangular Ducts: Comparison with Experiment," *Journal of Sound and Vibration*, Vol. 92, No. 3, 1984, pp. 387–409. doi:10.1016/0022-460X(84)90387-0

[15] Jones, M. G., Parrott, T. L., and Watson, W. R., "Comparison of Acoustic Impedance Eduction Techniques for Locally-Reacting Liners," 9th AIAA/CEAS Aeroacoustics Conference, AIAA Paper 2003-3306, 2003.

[16] Jones, M. G., Smith, W. R., Parrott, T. L., and Smith, C. D., "Design and Evaluation of Modifications to the NASA Langley Flow Impedance Tube," 10th AIAA/CEAS Aeroacoustics Conference, AIAA Paper 2004-2837, 2004.

[17] Watson, W. R., Jones, M. G., and Parrott, T. L., "A Quasi-3-D Theory for Impedance Eduction in Uniform Grazing Flow," AIAA/CEAS Aeroacoustics Conference, AIAA, Paper 2005-2848, May 2005.

[18] Howerton, B. M., and Parrott, T. L., "Validation of an Acoustic Impedance Prediction Model for Skewed Resonators," 15th AIAA/CEAS Aeroacoustics Conference and Exhibit, AIAA Paper 2009-3143, 2009.

[19] Watson, W. R., and Jones, M. G., "Impedance Eduction in Ducts With Higher-Order Modes And Flow," 15th AIAA/CEAS Aeroacoustics Conference and Exhibit, AIAA Paper 2009-3236, 2009.

[20] Tam, C. K. W., and Kurbatskii, K. A., "Microfuid Dynamics And Acoustics Of Resonant Liners," *AIAA Journal*, Vol. 38, No. 8, Aug. 2000, pp. 1331–1339. doi:10.2514/2.1132

[21] Tam, C. K. W., Kurbatskii, K. A., Ahuja, K. K., and Gaeta, R. J., Jr., "A Numerical and Experimental Investigation of the Dissipation Mechanisms of Resonant Acoustic Liners," *Journal of Sound and Vibration*, Vol. 245, No. 3, 2001, pp. 545–557. doi:10.1006/jsvi.2001.3571

[22] Tam, C. K. W., Ju, H., Jones, M. G., and Parrott, T. L., "A Computational and Experimental Study of Slit Resonators," *Journal of Sound and Vibration*, Vol. 284, Nos. 3–5, 2005, pp. 947–984. doi:10.1016/j.jsv.2004.07.013

[23] Tam, C. K. W., Ju, H., and Walker, B. E., "Numerical Simulation of a Slit Resonator in a Grazing Flow Under Acoustic Excitation," *Journal of Sound and Vibration*, Vol. 313, Nos. 3–5, Feb. 2008, pp. 449–471. doi:10.1016/j.jsv.2007.12.018

[24] Tam, C. K. W., Ju, H., Jones, M. G., Watson, W. R., and Parrott, T. L., "A Computational and Experimental Study of Resonators in Three Dimensions," AIAA/CEAS Aeroacoustics Conference, Miami, FL, AIAA Paper 2009-3171, May 2009.

[25] Eldredge, J. D., Bodony, D. J., and Shoeybi, M., "Numerical Investigation of the Acoustic Behavior of a Multi-Perforated Liner," 28th AIAA Aeroacoustics Conference, AIAA Paper 2007-3683, May 2007.

[26] Howe, M. S., "On the Theory of Unsteady High Reynolds Number Flow Through a Circular Aperture," *Proceedings of the Royal Society of London A*, Vol. 366, No. 1725, 1979, pp. 205–223. doi:10.1098/rspa.1979.0048

[27] Hersh, A. S., Walker, B. E., and Celano, J. W., "Helmohotz Resonator Impedance Model, Part 1: Nonlinear Behavior," *AIAA Journal*, Vol. 41, No. 5, May 2003, pp. 795–808. doi:10.2514/2.2041

[28] Rice, E. J., and Edward, J., "A Model for the Acoustic Impedance of a Perforated Plate with Multiple Frequency Excitation," NASA TM X-67950, 1971.

[29] Lele, S. K., "Compact Finite Difference Schemes with Spectral-Like Resolution," *Journal of Computational Physics*, Vol. 103, No. 1, 1992, pp. 16–42. doi:10.1016/0021-9991(92)90324-R

[30] Poinsot, T. J., and Lele, S. K., "Boundary Conditions for Direct Simulation of Compressible Viscous Flows," *Journal of Computational Physics*, Vol. 101, No. 1, April 1992, pp. 104–129. doi:10.1016/0021-9991(92)90046-2

[31] Bodony, D. J., "Characteristic Boundary Conditions for Non-Orthogonal, Moving Meshes," 47th Aerospace Sciences Meeting and Exhibit, AIAA Paper 2009-0010, Jan. 2009.

[32] Freund, J. B., "Proposed Inflow/Outflow Boundary Condition for Direct Computation of Aerodynamic Sound," *AIAA Journal*, Vol. 35, No. 4, April 1997, pp. 740–742. doi:10.2514/2.167

[33] Bodony, D. J., "Analysis of Sponge Zones for Computational Fluid Mechanics," *Journal of Computational Physics*, Vol. 212, No. 2, 2006, pp. 681–702. doi:10.1016/j.jcp.2005.07.014

[34] Zhang, Q., "Numerical Simulation of Two-Dimensional Acoustic Liners with High Speed Grazing Flow," M.S. Thesis, Department of Aerospace Engineering, Univ. of Illinois at Urbana-Champaign, Urbana, IL, 2010.

[35] Rowley, C. W., Colonius, T., and Basu, A. J., "On Self-Sustained Oscillations in Two-Dimensional Compressible Flow over Rectangular Cavities," *Journal of Fluid Mechanics*, Vol. 455, 2002, pp. 315–346. doi:10.1017/S0022112001007534

[36] Tam, C. K. W., and Auriault, L., "Time-Domain Impedance Boundary Conditions for Computational Aeroacoustics," *AIAA Journal*, Vol. 34, No. 5, 1996, pp. 917–923. doi:10.2514/3.13168

T. Jackson
Associate Editor